GAMMA RAY ATTENUATION OF THE M2/M3 BRADLEY FIGHTING VEHICLE

A Thesis
Presented to
The Academic Faculty

by

Desirée R. Prince

In Partial Fulfillment
Of the Requirements for the Degree
Master of Science in Nuclear and Radiological Engineering in the
Woodruff School of Mechanical Engineering

Georgia Institute of Technology

May 2018

GAMMA RAY ATTENUATION OF THE M2/M3 BRADLEY FIGHTING VEHICLE

Approved by:

Dr. Nolan E. Hertel, Advisor
The Woodruff School of Mechanical Engineering
Georgia Institute of Technology

Dr. Steven Biegalski
The Woodruff School of Mechanical Engineering
Georgia Institute of Technology

Dr. Paul A. Charp
The Woodruff School of Mechanical Engineering
Georgia Institute of Technology

Date Approved: April 23, 2018

To my mom, Tina, and my sister and brother, Talia and Shawn. There simply are not enough words to say what you mean to me, but in a word, “everything.”

ACKNOWLEDGEMENTS

First and foremost, I want to thank my Lord and Savior, Jesus Christ. Through Him, all things are possible.

Next, I would like to thank my advisor, Dr. Nolan Hertel, for taking me on as his student. Certainly, his support, guidance, and knowledge have made all the difference. I would also like to thank my committee members, Dr. Steven Biegalski and Dr. Paul Charp, for their support in working through even the most unusual of circumstances.

I would like to say a special thanks to Dr. C-K Chris Wang and Dr. Farzad Rahnema for their willigness to answer my questions and provide additional guidance on how to proceed on the project.

Many thanks to Dr. Michael Shannon and his team at the Georgia Tech Research Institute (GTRI) for allowing me to work on this project, and a debt of gratitute to my fellow students John Stooksbury, Caleigh Samuels, and Chad Burns, whose contributions have been invaluable.

Finally, thanks to Nicholas Antonio. As my colleauge, confidant, and "battle buddy," his support has been indispensible.

TABLE OF CONTENTS

LIST OF TABLES

LIST OF FIGURES

LIST OF SYMBOLS AND ABBREVIATIONS

^{131}I	iodine-131
^{137}Cs	cesium-137
^{14}C	carbon-14
^{226}Ra	radium-226
^{60}Co	cobalt-60
^{89}Sr	strontium-89
^{90}Sr	strontium-90
AN/VDR-2	Army, Navy/Vehicular (Ground), Radioactivity Detection, Indication, and Computation, Passive Detecting-2 (AN/VDR-2)
ANS	American Nuclear Society
ANSI	American National Standards Institute
CBRNE	Chemical, Biological, Radiological, Nuclear, and Explosives
CFR	Code of Federal Regulations
cGy	centigray
cm	centimeter
DoD	Department of Defense
GHz	gigahertz
GM	Geiger-Mueller
GTRI	Georgia Tech Research Institute
h	hour
ICRP	International Commission on Radiological Protection
ℓ	length
LANL	Los Alamos National Laboratory
m	meter

M2/M3 BFV	M2/M3 Bradley Fighting Vehicle
mCi	millicurie
MCNP	Monte Carlo N-Particle
MeV	megaelectron volt
NaI(Tl)	thallium-doped sodium iodide
NIST	National Institute of Standards and Technology
pSv	picosievert
R^2	coefficient of determination
RADIAC	Radioactivity Detection, Indication, and Computation
RAM	random access memory
s	second
SPAWAR	Space and Naval Warfare Systems Command
TM	technical manual
μ	Linear (dose) attenuation coefficient
μGy	microgray
σ	standard deviation (population)

SUMMARY

The United States Department of Defense (DoD) is working to develop newer and better tactical detectors. These detectors must be able to provide information about the radiological environment external the vehicle even while internally installed in vehicles such as the M2/M3 Bradley Fighting Vehicle (BFV). To this end, the gamma attenuation of the M2/M3 BFV must be characterized in order to develop attenuation settings which will allow the detector to translate the radiation intensity measured inside the vehicle into the radiation intensity outside of the vehicle. Essentially, the detector must be able to use the logic "if this (average) energy, then that attenuation coefficient" to display as its output the solution to the equation $I_0 = \frac{I}{B\, e^{-\mu \ell}}$ where I_0 is the radiation intensity just outside the walls of the M2/M3 BFV; I is the radiation intensity measured inside the M2/M3 BFV; B is the buildup factor of the materials in the M2/M3 BFV walls; μ is the dose attenuation coefficient of the vehicle's walls; and ℓ is the length of the absorber between the source and the detector in centimeters.

Dose attenuation coefficients for the walls of the M2/M3 Bradley Fighting Vehicle (BFV) were determined experimentally using cobalt-60 (^{60}Co), cesium-137 (^{137}Cs), and radium-226 (^{226}Ra). However, due to several assumptions being made about the vehicle's construct versus verified fact, an experiment of rudimentary design, numerous procedural missteps, use of a less than ideal detector, and use of inadequate sources, experimental determination was not successful: when the experimental data were compared to data generated using computational modeling via the Monte Carlo N-Particle (MCNP) Transport Code, the results did not agree well.

CHAPTER 1. INTRODUCTION

The 1945 debut of two nuclear weapons known as “Fat Man” and “Little Boy” brought about new requirements for battlefield capabilities for the United States’ military. Prior to World War II, battlefield detection primarily focused on chemical detection. However, the 1950s brought about an interest in developing a mobile chemical laboratory that was capable of detecting chemical, biological, and radiological agents. A series of radiological detection developments would continue until 1988 when the Department of Defense (DoD) finalized development of the Army, Navy/Vehicular (Ground), Radioactivity Detection, Indication, and Computation (RADIAC), Passive Detecting-2 (AN/VDR-2) (Smart 21).

Figure 1.1. The AN/VDR-2 with DT-616 probe (*Argon Electronics*)

Initially fielded in 1989, the AN/VDR-2 is a survey instrument fitted with the DT-616 probe, a Geiger-Muller (GM) device containing one tube that acts as a low-range detector (0.01 μGy/h to 5 cGy/h) for both beta and gamma radiation and an additional tube for high-range gamma detection (2cGy/h to 100 Gy/h) (Eastburg 14). The detector

may be carried as a man-portable instrument or installed in many of the tracked and wheeled vehicles that comprise the military's fleet. However, the DoD has recently endeavored to update its services' chemical, biological, radiological, nuclear, and explosives (CBRNE) inventory for with newer, more reliable detectors that have greater ease of use and that give detection system operators real-time feedback about the radiological environment outside of their vehicle rather than providing information about conditions inside the vehicle. As such, the gamma attenuation tendencies of a vehicle into which the detector will be installed must be characterized in order to determine how much the radiation's intensity will have been decreased before reaching a vehicle-internal detector. Essentially, the detector must be able to use the logic "if this (average) energy, then that attenuation coefficient" to display as its output the solution to the equation $I_0 = \frac{I}{B\, e^{-\mu \ell}}$ where I_0 is the radiation intensity just outside the walls of the vehicle; I is the radiation intensity measured inside the vehicle; B is the buildup factor of the materials in the M2/M3 BFV walls; μ is the linear attenuation coefficient of the vehicle's walls; and ℓ is the length of the absorber between the source and the detector in centimeters.

The objective of this thesis is to determine the gamma attenuation characteristics of the M2/M3 Bradley Fighting Vehicle (BFV), a lightly armored, tracked combat vehicle primarily used by the US Army's mechanized infantry and armored cavalry soldiers, using the AN/VDR-2 and three sources—cobalt-60 (^{60}Co), cesium-137 (^{137}Cs), and radium-226 (^{226}Ra). Attenuation characteristics will be determined using experimental, analytical, and computational methods. The Monte Carlo N-Particle Transport (MCNP) Code will be used to determine the computational attenuation characteristics.

Experiments and computations in this thesis are rudimentary at best and require significant improvement in future works.

Figure 1.2. The M2/M3 Bradley Fighting Vehicle (*American Military History* 328)

CHAPTER 2. THEORY AND BACKGROUND

2.1 The Linear Attenuation Coefficient

The linear attenuation coefficient is a value which can be interpreted as the probability of a photon experiencing a collision as it travels through a medium (Wang 256) or alternatively, "the fraction of a beam of [rays] that is absorbed or scattered per unit thickness of the absorber" ("Transmitted Intensity"). The linear attenuation coefficient for a narrow, collimated beam of monoenergetic photons is given by the equation

$$\mu = -\frac{1}{\ell} ln\left(\frac{I}{I_0}\right) \quad \textbf{(2.1)}$$

where ℓ is the thickness of the absorber in centimeters, I is the intensity of the photons that have been transmitted across a distance ℓ, and I_0 is the initial intensity of the incident beam of photons. Experimentally, one can easily and simply determine the linear attenuation coefficient by collimating a gamma photon source, recording the intensity as the beam of photons reaches the detector (that is, I_0), placing a medium of interest in the path of the collimated beam and recording the intensity (that is, I), and using the above equation, determine the value for the linear attenuation (Poškus 9). Such is the basis for this elementary experiment. While one may usually find the linear attenuation coefficient for a given material in an appropriate compendium or database such as the National Institute of Standards and Technology's (NIST) XCOM Photon Cross Section Database, this problem is unique in that the true identity of the materials used to construct the M2/M3 BFV are classified and restricted to those only with the appropriate clearance

level and a need to know. Considering this, it becomes necessary to determine the attenuation coefficient experimentally, though taking an analytic or computational approach using "best guesses" based on information that is available from open sources can certainly be used to refine subsequent experiments.

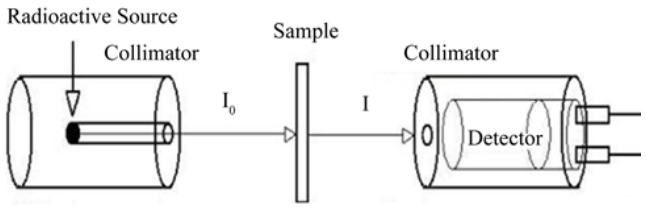

Figure 2.1. Typical setup for an experimental linear attenuation coefficient determination (Madbouly 271)

2.2 The M2/M3 BFV

As previously mentioned, the true identity of the materials which comprise the M2/M3 BFV is unavailable to the researcher for this problem. However, one can reasonably observe that the M2/M3 BFV is constructed of some sort of metal or metal alloy and moving forward in defining the problem, review open sources with an eye for those that are based on materials such as steel or other hardened, comparatively low-cost alloys. Following a period of research, the researcher has elected to use the following as a basis for this problem—

> The hull vertical sides and rear armor consisted of two .25" (.64 cm) steel plates one inch (2.5 cm) apart and 3.5" (8.9 cm) away from the aluminum armor. The hull top, bottom, and front consisted of 5083 aluminum armor,

and .375" (.953 cm) steel armor was added to the front third of the hull bottom to increase mine protection (Connors).

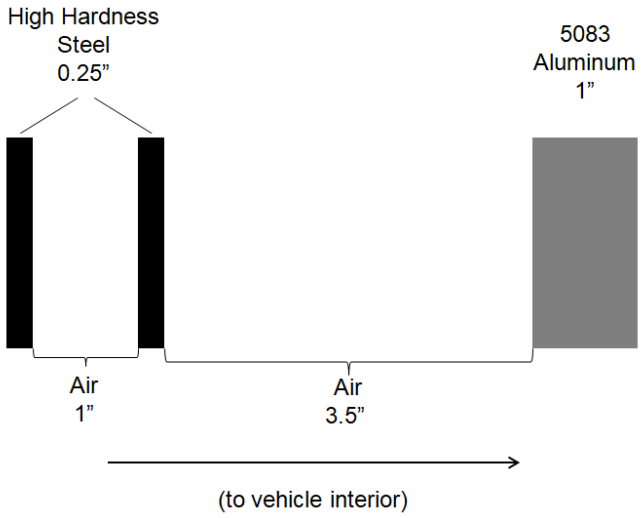

Figure 2.2. Diagram of the walls of the M2/M3 Bradley Fighting Vehicle (not to scale)

Two additional open sources suggest a similar construct and provide a validation of sorts—

> The hull and turret on the Bradley were assembled from 5083 and 7039 aluminum alloy armor combined with steel spaced laminate armor. The latter consisted of two 1/4 inch thick, high hardness, steel plates spaced one inch apart and mounted 3 1/2 inches outboard of the one inch thick aluminum armor (Hunnicut).

and

> The entire Bradley is covered with aluminum armor, and the rear and sides are also covered with spaced laminate armor. The turret has an additional layer of steel, and the hull bottom has additional anti-mine armor (Bonsor).

It is reasonable to assume that aluminum 5083 has, indeed, been used in the construct of the M2/M3 BFV, as this alloy may be welded without a reduction in strength and is often used in building vehicles (*Aluminum Alloys*). The M2/M3 BFV, indeed, has a welded hull, and it therefore seems probable that, considering the use and the aforementioned property of the aluminum 5083, one could select this material for such an application. In selecting a steel to consider, high hardness steel is a reasonable selection, as the DoD has published a military detail outlining the required specifications for this material as an armor (*Detail Specification*).

An additional consideration for the attenuation characteristics of the M2/M3 BFV is its engine. The engine block is a considerably large metal structure that has the potential to provide significant attenuation based on its suspected composition of cast iron. Again, this is another component with relatively few details available on open source due to security requirements. However, one open source indicates that the engine is a Cummins VTA-903T model (Pike). Further research uncovered an author that includes a similar, civilian model, the Cummins VTA-903, in his blanket term "heavy iron." That is, a cast iron engine where "weight and overall size where not really the focus of the design" (Athens). Thus, one may make the assumption that the engine installed in the M2/M3 BFV is likely to be constructed of cast iron as well. Gray iron, a type of cast iron, is often used in engine blocks because of its resistance to wear

("Introduction to Cast Iron"). It seems logical to proceed under the assumption that the engine installed in the M2/M3 BFV is constructed of gray iron.

Table 2.1. Materials Impacting the M2/M3 BFV Dose Attenuation Coefficient

Material	Density (g/cm^3)	Component	Composition Percentage (%)
Air	1.18×10^{-3}	Nitrogen	78.080
		Oxygen	20.980
		Argon	0.930
		Carbon	0.010
Aluminum 5083	2.65	Aluminum	93.400
		Magnesium	4.450
		Manganese	0.700
		Silicon	0.400
		Iron	0.400
		Zinc	0.250
		Titanium	0.150
		Chromium	0.150
		Copper	0.100
Steel	8.05	Iron	99.027
		Carbon	0.320
		Copper	0.250
		Aluminum	0.100
		Titanium	0.100
		Zirconium	0.100
		Phosphorus	0.020
		Arsenic	0.020
		Tin	0.020
		Antimony	0.020
		Sulfur	0.010
		Lead	0.010
		Boron	0.003
Cast Iron	7.34	Iron	93.415
		Carbon	3.250
		Silicon	2.000
		Phosphorus	0.600
		Manganese	0.600
		Sulfur	0.135

2.3 The AN/VDR-2 and the ^{60}Co, ^{137}Cs, and ^{226}Ra Sources

As previously stated, the detector used for this experiment is one that is currently in service in DoD's inventory—the AN/VDR-2—and is capable of detecting gamma and beta emissions using the DT-616 probe, a GM device. A GM device's simplistic design is capable of audibly detecting radiation "as it passes through the GM tube [and] ionizes the gas within the tube. This ionization creates a momentary conductive path between the wire at the center of the tube… and the wall of the tube… The momentary conductive path creates an electrical pulse that results in a 'click' sound. This conductive path is quickly quenched by the halogen gas inside the GM tube" ("How Geiger Counters Work"). Users are then able to read the pulse count from the GM counter's display. GM devices are generally acceptable for use with beta and gamma emitters, though some models are capable of detecting alpha emissions as well.

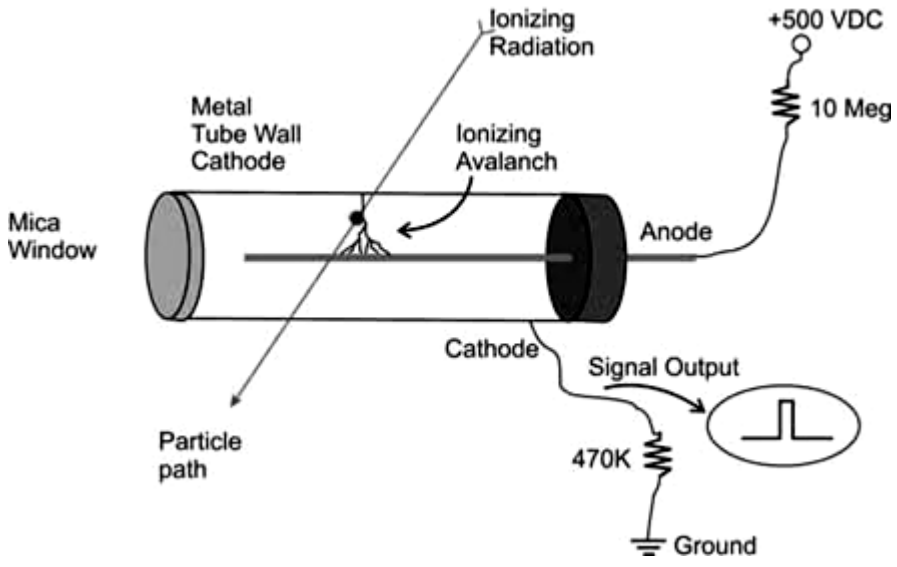

Figure 2.3. Schematic of a typical Geiger-Mueller tube ("How Geiger Counters Work")

For the purposes of this experiment, only gamma photons have been considered: beta particles, or energized electrons, generally only travel short distances in matter (on the order of feet) before losing significant amounts of energy to inelastic collisions (Wang 232). More importantly, one would reasonably expect the walls of the M2/M3 BFV to effectively shield the internally located detector from any sort of beta emissions, as thin layers of metal or plastic can sufficiently stop a beta particle ("Radiation Basics").

Gamma-emitting sources that were chosen for this experiment include ^{60}Co with an activity of 10.0 mCi, ^{137}Cs with an activity of 82.3 mCi, and ^{226}Ra with an activity of 10.0 mCi. In reviewing the decay schemes for each of the nuclides, one finds that they are generally acceptable for use as gamma emitters covering a range of energies with ^{60}Co emitting gamma photons at 1.173 MeV and 1.332 MeV for weighted average photon energy of 1.253 MeV; ^{137}Cs emitting gamma photons at 0.662 MeV; and ^{226}Ra emitting gamma photons at 0.186 MeV, 0.262 MeV, and 0.601 MeV for a weighted average photon energy of 0.190 MeV.

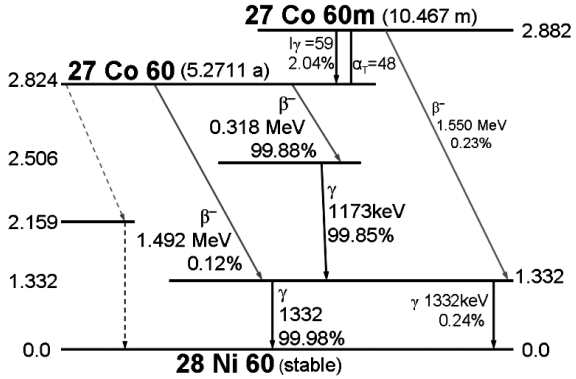

Figure 2.4. Decay scheme for cobalt-60 ("Co 60 Decay Scheme")

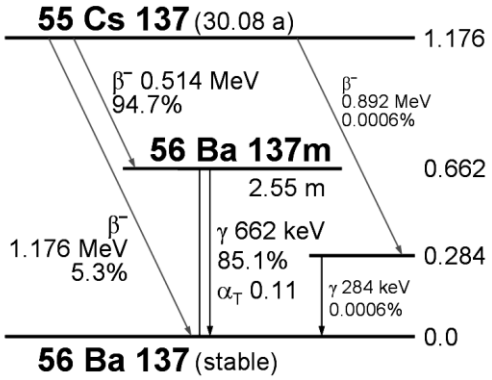

Figure 2.5. Decay scheme for cesium-137 ("Cs 137 Decay Scheme")

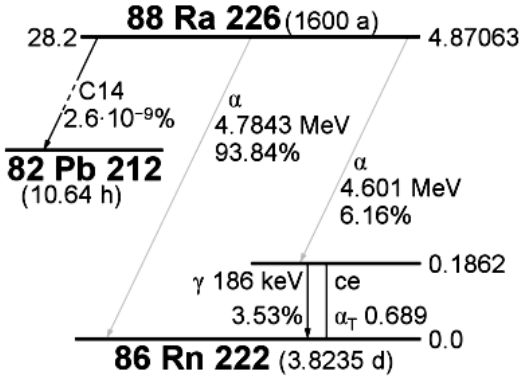

Figure 2.6. Decay scheme for radium-226 ("Ra 226 Decay Scheme")

2.4 The MCNP Transport Code for Computational Modeling

The MCNP Transport Code is a "radiation-transport code designed to track many particle types over broad ranges of energies" (Pelowitz 1-1). Employing the Monte Carlo method as indicated by its name, MCNP uses random numbers in conjunction with a probabilistic model in order to obtain simulations of three-dimensional radiation transport problems. In general, MCNP requires the user to define the problem using three

blocks of cards—the cell and the surface blocks to specify the geometry of the problem and the data block to specify the particles of interest for the problem, the source's parameters, the required outputs (tallies), the composition of the materials in the problem, and conditions for run termination. Developed by Los Alamos National Laboratory (LANL), MCNP has come to be regarded as an industry standard computational modeling code for application areas that include reactor design, medical physics, dosimetry and detection, and shielding design (Pelowitz 1-5).

CHAPTER 3. EXPERIMENTAL METHODOLOGY AND PROCEDURES

The M2/M3 BFV was made available by the US Army Armor School located at Fort Benning, Georgia where this experiment was conducted. The AN/VDR-2 was provided by the San Diego, California-based Space and Naval Warfare Systems Command (SPAWAR). All sources were acquired by the Georgia Tech Research Institute (GTRI) Advanced Concepts Laboratory.

The area around the M2/M3 BFV was clearly marked with a masking tape grid indicating the positions at which the source was to be placed during the experiment. Each position was marked 100 cm from the outermost wall of the M2/M3 BFV.

The attenuation factor on the AN/VDR-2 should have been set to 1.0 per the steps outlined in *Technical Manual (TM) No. 11-6665-251-20 Organizational Maintenance Manual RADIAC Set AN/VDR-2* to ensure that the AN/VDR-2 did not adjust outputs for the attenuation characteristics of a vehicle into which it may have been installed. However, this step was not completed, and the researcher is unable to verify that dose rate measurements taken during this experiment are accurate and true, though measurements do provide some information that is useful relative to other dose rate measurements recorded during the experiment. The AN/VDR-2 was then installed as outlined in the aforementioned manual, and preoperational test procedures were conducted in accordance with *TM No. 11-6665-251-10 Operator's Manual RADIAC Set AN/VDR-2*. No operational issues were discovered during preoperational testing. Upon completion of installation, the vehicle's rear ramp and driver's hatch were left open.

Select dimensional measurements were taken for the M2/M3 BFV, AN/VDR-2, and source.

Table 3.1. Dimensional Measurements for the Experiment Setup

Parameter	Measurement (cm)
AN/VDR-2 distance from the nearest exterior (left) wall	39.40
AN/VDR-2 distance from the rear of the M2/M3 BFV	321.31
AN/VDR-2 distance from the ground	151.77
M2/M3 BFV width	320.00
M2/M3 BFV length	593.00
Source height	128.27

The ^{60}Co source was placed on a wooden cart and was imperfectly collimated using lead bricks. A plumb bob was centered and attached beneath the source to ensure proper placement during the experiment. The source was rotated so that the beam faced away from the vehicle and was removed from each position by no more than 150-200 cm when taking background radiation measurements. The background radiation measurement was recorded in the absorbed dose rate unit μGy/h after 180 s elapsed to allow the pulse count to stabilize. The source was then rotated so that the beam was aimed at the detector. The source measurement was also recorded in the absorbed dose rate unit μGy/h after 180 s elapsed. The exact angle of the beam to the detector was not measured or recorded.

These steps were repeated for each of the twelve marked positions and one additional position located under the vehicle. The steps were then repeated for the remaining two sources—^{226}Ra first, then ^{137}Cs. After all measurements were taken with the detector installed in the vehicle, the experiment was repeated with the detector placed on an adjustable shelving unit to simulate the placement of the detector when properly

installed the M2/M3 BFV, though the pulse rate was only allowed to stabilize for 60 s for ^{60}Co and ^{226}Ra and 30 s for ^{137}Cs.

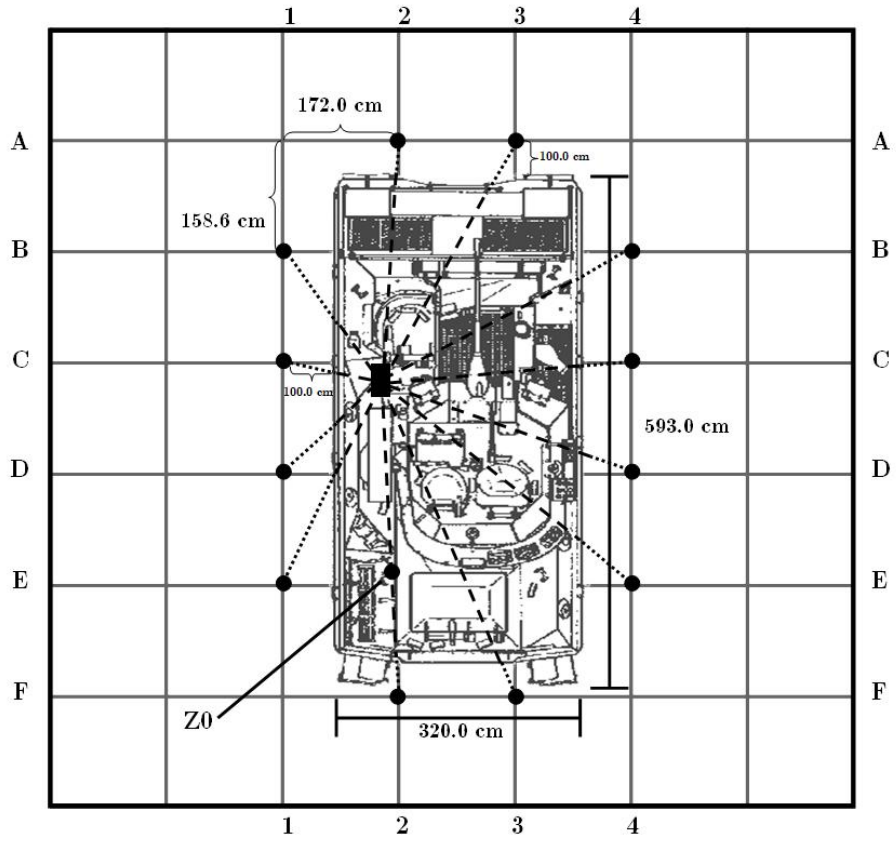

Figure 3.1. Experimental Setup (not to scale)

CHAPTER 4. EXPERIMENTAL DATA ANALYSIS AND RESULTS

4.1 The Net Absorbed Dose Rate

The data collected from this experiment is consistent with what one might typically expect from such a simple experiment design that is procedurally flawed, though overall, the data does reflect some consistent trends for each source. Data tabulated below includes the background count, the source count, and the net count (that is, the source count minus the background count) for each source. Two data sets are presented for each source—one data set for measurements taken with the detector internally located and one set for the measurements taken with the detector located outside of the M2/M3 BFV but placed in an identical position.

In reviewing the data, one immediately notices that two of the sources have negative net absorbed dose rates for measurements taken with the detector installed internally: ^{60}Co has negative net absorbed dose rates associated with positions E1, E4, and F3, while ^{137}Cs has negative net absorbed dose rates associated with positions A2 and A3. One hypothesis for these seeming anomalies is that source was allowed to remain too close to the vehicle during background radiation counting: the sources were shielded with lead bricks and angled away from the vehicle, though they remained in relatively close proximity to the vehicle and were never removed more than 150-200 cm. For energetic sources such as ^{60}Co and even ^{137}Cs, it appears as though the lead bricks did not

provide adequate shielding for the sources: only the ^{226}Ra, the least energetic of the sources, was without negative net absorbed dose rate measurements.

(continued on next page)

Table 4.1. Experimental Absorbed Dose Data for ^{60}Co – Detector Internally Installed in the M2/M3 BFV

Position	Background Absorbed Dose Rate (µGy/h)	Source Absorbed Dose Rate (µGy/h)	Net Absorbed Dose Rate (µGy/h)
A2	1.94	2.96	1.02
A3	1.77	4.30	2.53
B4	1.77	2.39	0.62
C4	1.91	2.28	0.37
D4	1.74	1.98	0.24
E4	1.80	1.70	-0.10
F3	1.90	1.81	-0.09
F2	1.77	1.89	0.12
E1	2.36	2.12	-0.24
D1	1.79	4.67	2.88
C1	1.99	8.08	6.09
B1	2.63	3.26	0.63
Z0	1.87	7.87	6.00

Table 4.2. Experimental Absorbed Dose Data for ^{60}Co – Detector Located Outside of the M2/M3 BFV in an Identical Position

Position	Background Absorbed Dose Rate (µGy/h)	Source Absorbed Dose Rate (µGy/h)	Net Absorbed Dose Rate (µGy/h)
A2	0.41	21.50	21.09
A3	0.30	15.80	15.50
B4	0.38	13.10	12.72
C4	0.50	13.60	13.10
D4	0.42	9.24	8.82
E4	0.43	5.45	5.02
F3	0.43	2.86	2.43
F2	0.49	2.39	1.90
E1	0.37	4.83	4.46
D1	0.41	10.80	10.39
C1	0.69	25.50	24.81
B1	0.39	26.60	26.21

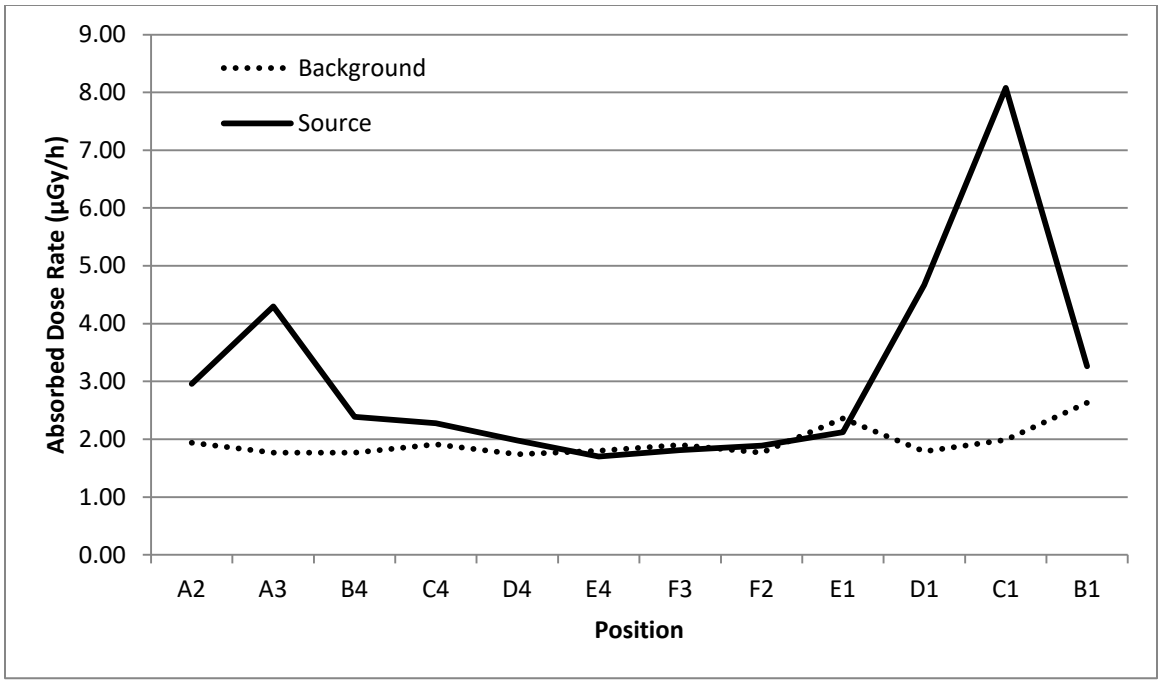

Figure 4.1. Plot of Position vs. Experimental Net Absorbed Dose Rate for ^{60}Co – Detector Internally Installed in the M2/M3 BFV

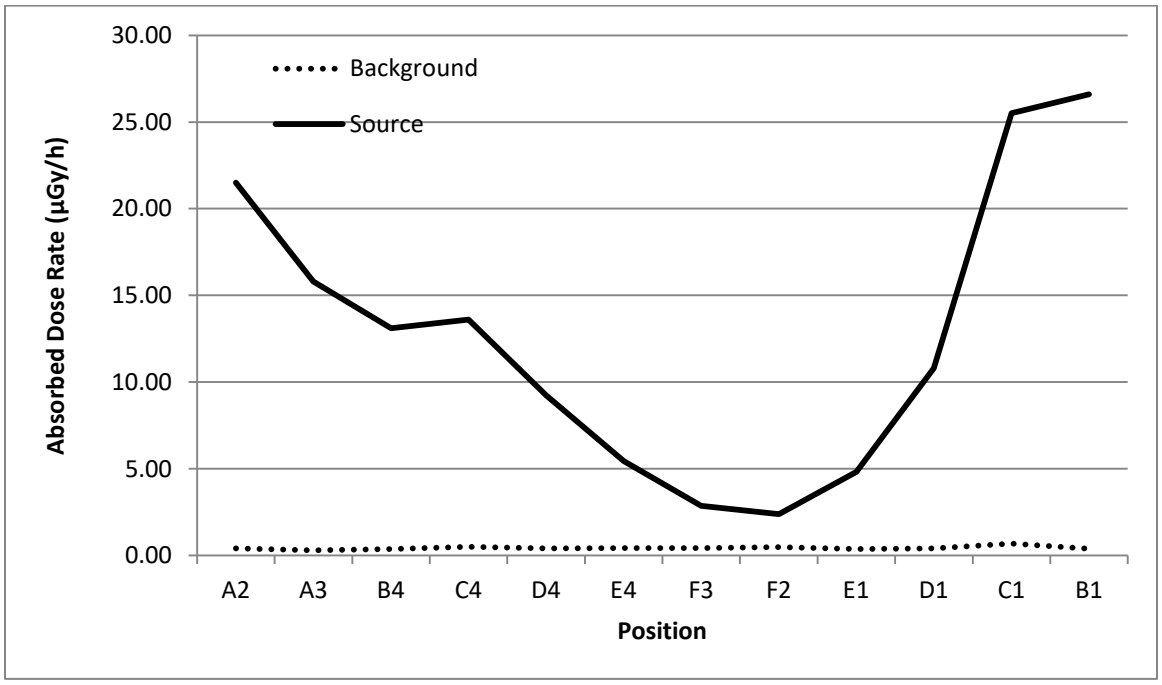

Figure 4.2. Plot of Position vs. Experimental Net Absorbed Dose Rate for ^{60}Co – Detector Located Outside of the M2/M3 BFV in an Identical Position

Table 4.3. Experimental Absorbed Dose Data for ^{137}Cs – Detector Internally Installed in the M2/M3 BFV

Position	Background Absorbed Dose Rate (µGy/h)	Source Absorbed Dose Rate (µGy/h)	Net Absorbed Dose Rate (µGy/h)
A2	1.89	1.75	-0.14
A3	1.75	1.69	-0.06
B4	1.67	1.72	0.05
C4	1.78	1.94	0.16
D4	1.69	2.20	0.51
E4	1.57	1.82	0.25
F3	1.67	4.38	2.71
F2	1.83	3.80	1.97
E1	1.62	1.92	0.30
D1	1.56	3.82	2.26
C1	1.54	9.56	8.02
B1	1.53	2.89	1.36
Z0	1.76	6.33	4.57

Table 4.4. Experimental Absorbed Dose Data for ^{137}Cs – Detector Located Outside of the M2/M3 BFV in an Identical Position

Position	Background Absorbed Dose Rate (µGy/h)	Source Absorbed Dose Rate (µGy/h)	Net Absorbed Dose Rate (µGy/h)
A2	0.43	37.20	36.77
A3	0.79	30.10	29.31
B4	0.69	24.20	23.51
C4	0.40	24.60	24.20
D4	0.42	15.40	14.98
E4	0.32	9.03	8.71
F3	0.48	3.45	2.97
F2	0.24	3.03	2.79
E1	0.34	6.91	6.57
D1	0.38	48.00	47.62
C1	0.40	48.00	47.60
B1	0.49	49.50	49.01
Z0			

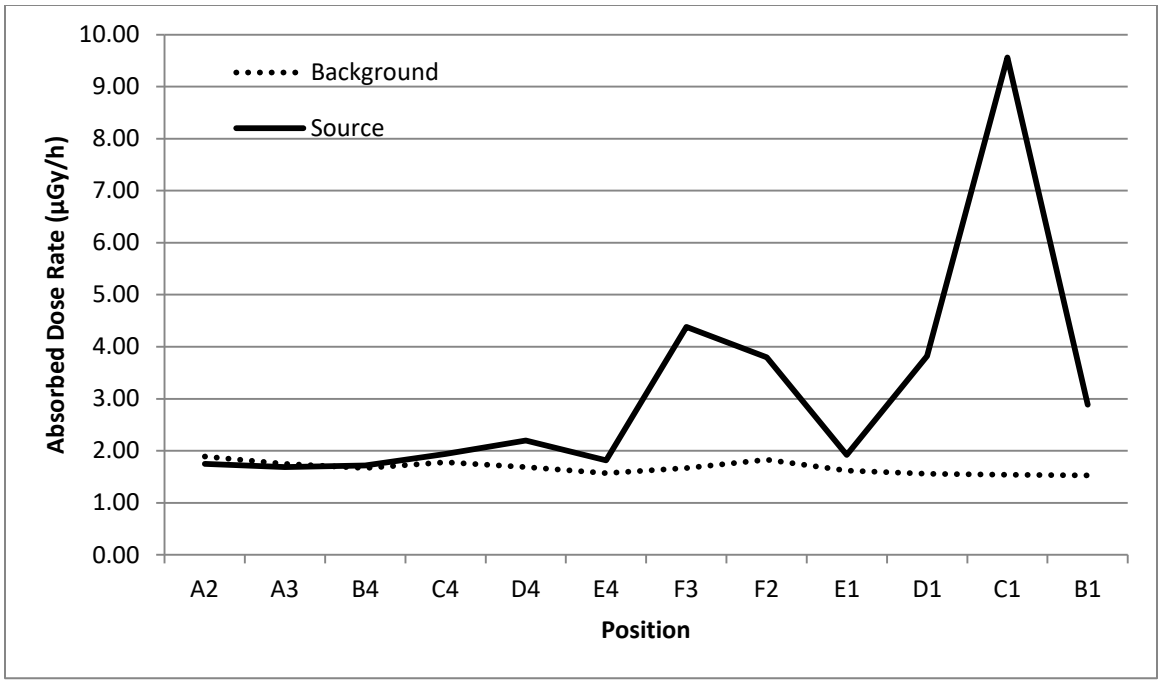

Figure 4.3. Plot of Position vs. Experimental Net Absorbed Dose Rate for ^{137}Cs – Detector Internally Installed in the M2/M3 BFV

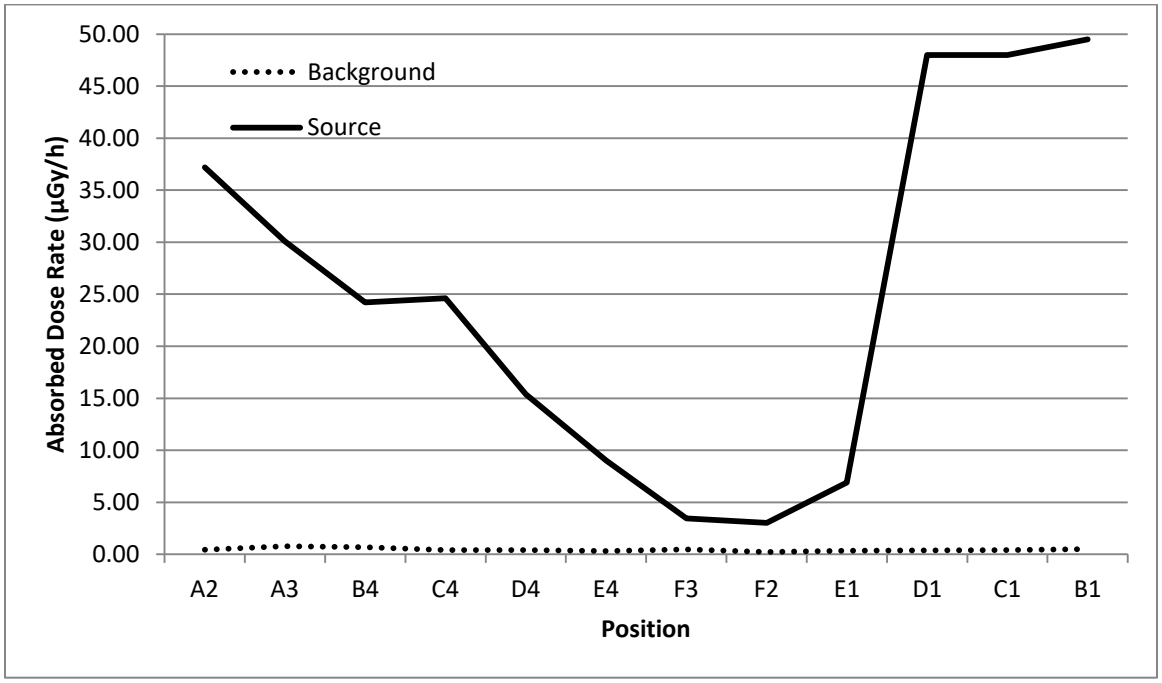

Figure 4.4. Plot of Position vs. Experimental Net Absorbed Dose Rate for ^{137}Cs – Detector Located Outside of the M2/M3 BFV in an Identical Position

Table 4.5. Experimental Absorbed Dose Data for ^{226}Ra – Detector Internally Installed in the M2/M3 BFV

Position	Background Absorbed Dose Rate (µGy/h)	Source Absorbed Dose Rate (µGy/h)	Net Absorbed Dose Rate (µGy/h)
A2	2.45	2.62	0.17
A3	1.97	3.96	1.99
B4	2.07	2.11	0.04
C4	2.15	2.45	0.30
D4	1.89	2.28	0.39
E4	1.96	2.00	0.04
F3	1.54	1.98	0.44
F2	1.98	1.99	0.01
E1	2.10	2.23	0.13
D1	1.91	4.06	2.15
C1	2.14	6.87	4.73
B1	1.98	2.97	0.99
Z0	1.95	7.87	5.92

Table 4.6. Experimental Absorbed Dose Data for ^{226}Ra – Detector Located Outside of the M2/M3 BFV in an Identical Position

Position	Background Absorbed Dose Rate (µGy/h)	Source Absorbed Dose Rate (µGy/h)	Net Absorbed Dose Rate (µGy/h)
A2	0.59	13.70	13.11
A3	0.47	11.10	10.63
B4	0.46	9.68	9.22
C4	0.41	9.28	8.87
D4	0.27	5.88	5.61
E4	0.44	3.69	3.25
F3	0.46	2.22	1.76
F2	0.44	1.74	1.30
E1	0.57	3.62	3.05
D1	0.48	7.87	7.39
C1	0.48	16.10	15.62
B1	0.46	17.80	17.34
Z0			

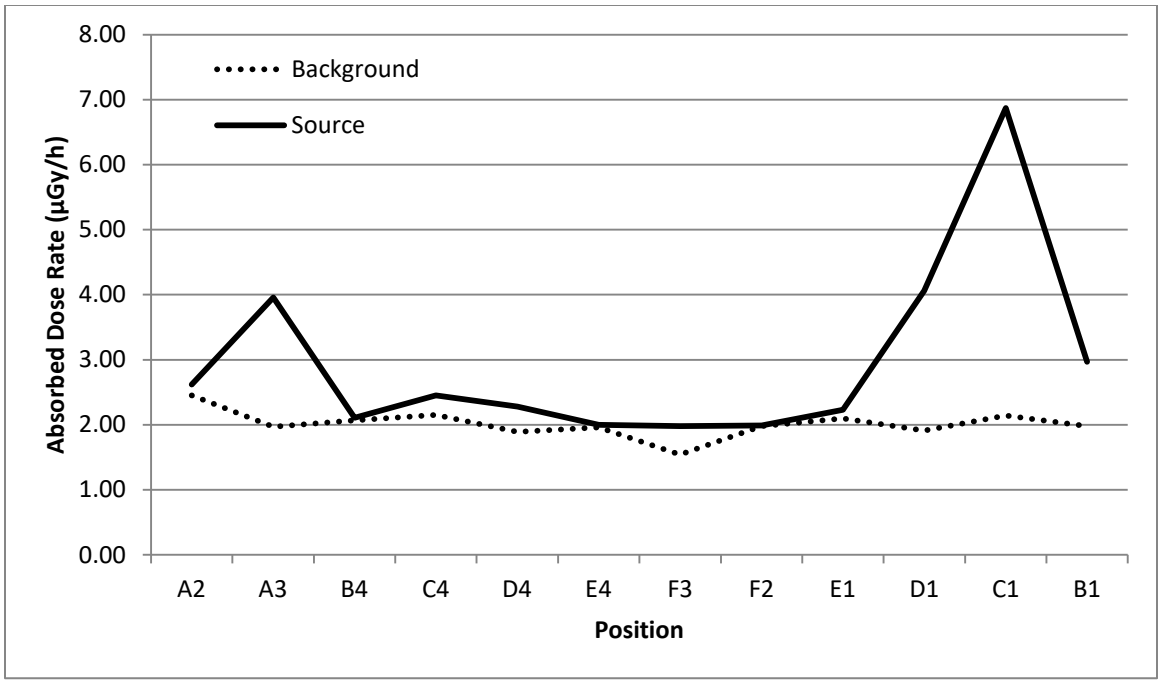

Figure 4.5. Plot of Position vs. Experimental Net Absorbed Dose Rate for ^{226}Ra – Detector Internally Installed in the M2/M3 BFV

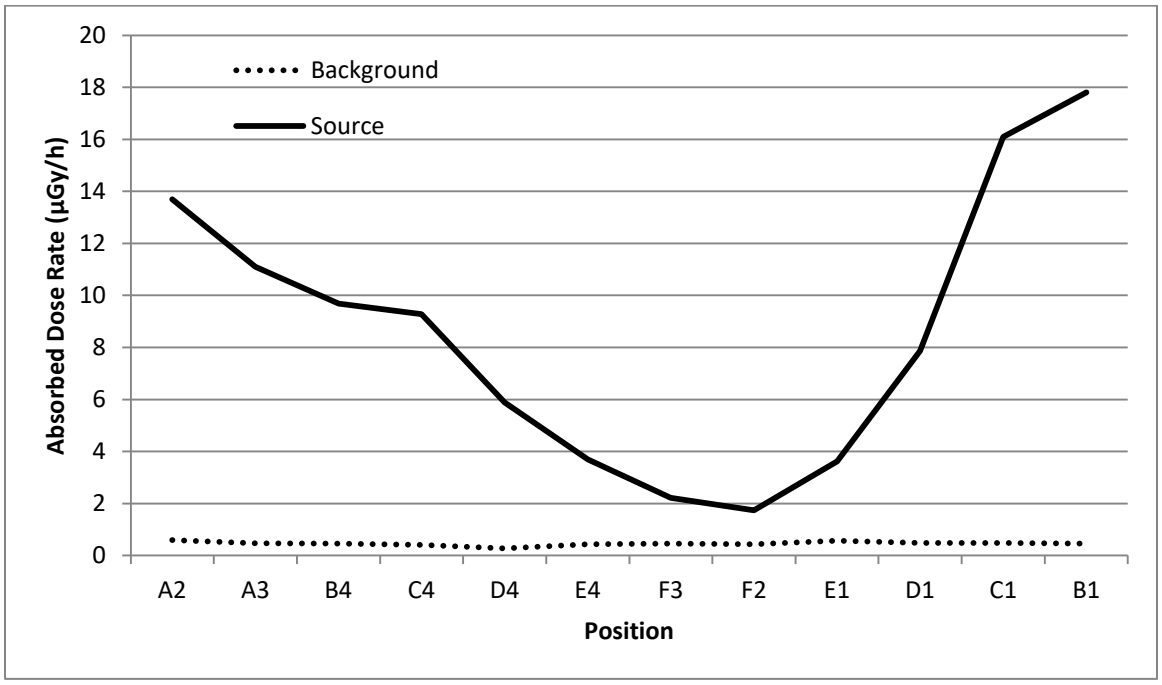

Figure 4.6. Plot of Position vs. Experimental Net Absorbed Dose Rate for ^{226}Ra – Detector Located Outside of the M2/M3 BFV in an Identical Position

Also of note, there are some positions where the background radiation measurements do not vary much from the source effects measurements. Consider for example the positions B4, E4, and F2 associated with the ^{226}Ra measurements taken with the detector installed in the vehicle. The difference for position F2 is 0.01 μGy/h, and the difference for positions B4 and E4 is 0.04 μGy/h. This lends some skepticism to the significance of these values and seems to suggest that sources used did not have a high enough activity to sufficiently penetrate such a well-armored vehicle for these measurements.

One also notices that background radiation is higher when measurements are taken in the presence of the M2/M3 BFV, usually on the order of 1 μGy/h or more, though this occurrence is not altogether surprising or problematic: the M2/M3 BFV's armament is capable of firing armor-piercing rounds which often contain depleted uranium. Additionally, the DoD has used depleted uranium for armor plating on its combat vehicles. It stands to reason that background radiation measurements taken in the presence of the M2/M3 BFV should, indeed, have higher values than those taken in the absence of the vehicle, and this seemingly unusual trend is not truly so unusual.

In reviewing the plots of position versus net absorbed dose rates, one finds that based on the shape, the curves for each of the sources agree considerably well. Notably, position C1, the position with the shortest distance from the source to the detector, consistently has the highest measurement which is consistent with what one would expect given Isaac Newton's inverse-square law that "accounts for the fact that radiation becomes weaker as it spreads out over a larger area" ("Radiographic Inspection"). The inverse-square law is given by the equation

$$I_1 {D_1}^2 = I_2 {D_2}^2 \quad \textbf{(4.1)}$$

where I_1 is the intensity at some distance D_1; D_1 is the distance from the source; I_2 is the intensity at some distance D_2, and D_2 is the distance from the source. However, this point is debatable, as the dose in this case has been attenuated rather than the number of particles as given by the associated flux or fluence.

4.2 Calculating the Experimental Dose Attenuation Coefficient

As stated earlier, the linear attenuation coefficient, henceforth referred to as the dose attenuation coefficient for this experiment, is calculated using the equation $\mu = -\frac{1}{\ell} ln\left(\frac{I}{I_0}\right)$. For this experiment, the dose attenuation coefficient was calculated for each position for with ℓ being set to the distance from the source to the detector; I being set equal to the net absorbed dose rate for the measurements taken with the AN/VDR-2 internally installed in the M2/M3 BFV; and I_0 being set equal to the net absorbed dose rate for the measurements taken with the AN/VDR-2 located outside of the vehicle placed in an identical position. Note that dose attenuation coefficients for the position Z0 have not been calculated, as measurements with the detector located outside of the M2/M3 BFV in an identical position were not taken for this position. An entry of "INSF" indicates that there was insufficient data to calculate the dose attenuation coefficient. That is, the net absorbed dose rate is negative, which renders the equation for calculating the dose attenuation coefficient unusable due to the equation's logarithmic nature.[*]

[*]See Appendix E for additional dose attenuation coefficients calculated using the trimmed mean of the background absorbed dose rate.

In reviewing the dose attenuation coefficients calculated experimentally, it is difficult to note the trends one usually expects: ^{60}Co as the most energetic source does not consistently have the smallest dose attenuation coefficient. When compared to ^{137}Cs, the only positions at which ^{60}Co has a smaller dose attenuation coefficient are B4, C1, C4, and D1. When compared to ^{226}Ra, the only positions at which ^{60}Co generates a smaller dose attenuation coefficient are A2, B4, and F2. Similar inconsistencies can be noted when comparing ^{137}Cs and ^{226}Ra; consider positions B1, B4, C1, C4, D1, and D4. These irregularities, among others, further diminish confidence in the measurements observed in the experiment.

Table 4.7. Experimental Dose Attenuation Coefficients for ^{60}Co

Position	ℓ (cm)	I (μGy/h)	I_0 (μGy/h)	μ
A2	374.11	1.02	21.09	0.00810
A3	425.96	2.53	15.50	0.00426
B4	436.88	0.62	12.72	0.00692
C4	385.26	0.37	13.10	0.00926
D4	395.34	0.24	8.82	0.00912
E4	463.11	INSF	5.02	ISNF
F3	469.87	INSF	2.43	INSF
F2	423.43	0.12	1.90	0.00652
E1	298.40	INSF	4.46	INSF
D1	175.70	2.88	10.39	0.00730
C1	151.67	6.09	24.81	0.00926
B1	255.82	0.63	26.21	0.01457

Table 4.8. Experimental Dose Attenuation Coefficients for ^{137}Cs

Position	ℓ (cm)	I (µGy/h)	I_0 (µGy/h)	μ
A2	374.11	INSF	36.77	INSF
A3	425.96	ISNF	29.31	INSF
B4	436.88	0.05	23.51	0.01408
C4	385.26	0.16	24.20	0.01303
D4	395.34	0.51	14.98	0.00855
E4	463.11	0.25	8.71	0.00767
F3	469.87	2.71	2.97	0.00019
F2	423.43	1.97	2.79	0.00082
E1	298.40	0.30	6.57	0.01034
D1	175.70	2.26	47.62	0.01735
C1	151.67	8.02	47.60	0.01174
B1	255.82	1.36	49.01	0.01401

Table 4.9. Experimental Dose Attenuation Coefficients for ^{226}Ra

Position	ℓ (cm)	I (µGy/h)	I_0 (µGy/h)	μ
A2	374.11	0.17	13.11	0.01162
A3	425.96	1.99	10.63	0.00393
B4	436.88	0.04	9.22	0.01245
C4	385.26	0.3	8.87	0.00879
D4	395.34	0.39	5.61	0.00674
E4	463.11	0.04	3.25	0.00950
F3	469.87	0.44	1.76	0.00295
F2	423.43	0.01	1.30	0.01150
E1	298.40	0.13	3.05	0.01057
D1	175.70	2.15	7.39	0.00703
C1	151.67	4.73	15.62	0.00788
B1	255.82	0.99	17.34	0.01119

4.3 Calculating the Analytical Dose Attenuation Coefficient

As a basis for comparison, the dose attenuation coefficient for each source at each position was calculated by using each position's I_0 value and inverse-square law to

determine the intensity just at the outer wall of the M2/M3 BFV, I_1. Rearranging the equation $\mu = -\frac{1}{\ell} ln\left(\frac{I}{I_0}\right)$ into the form $I = I_0 e^{-\mu\ell}$ and using theoretical, NIST XCOM linear attenuation coefficients, the final intensity, $I_{7,}$ was calculated as depicted in Figure 4.7. The dose attenuation coefficient for the M2/M3 BFV wall was then determined using the intensities I_1 and $I_{7.}$

(continued on next page)

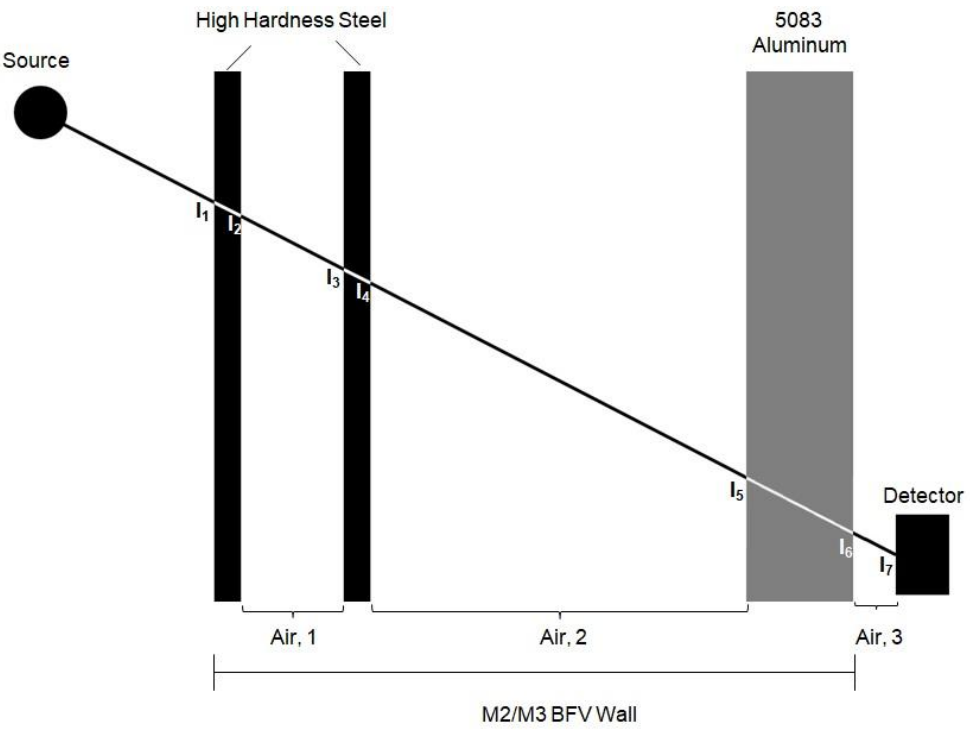

$$I_1 = \frac{I_0 {D_0}^2}{{D_1}^2}$$

$$I_2 = I_1 e^{-\mu_{steel}\ell_{steel}}$$

$$I_3 = I_2 e^{-\mu_{air}\ell_{air,1}}$$

$$I_4 = I_3 e^{-\mu_{steel}\ell_{steel}}$$

$$I_5 = I_4 e^{-\mu_{air}\ell_{air,2}}$$

$$I_6 = I_5 e^{-\mu_{Al5083}\ell_{Al5083}}$$

$$I_7 = I_6 e^{-\mu_{air}\ell_{air,3}}$$

$$\mu_{wall} = -\frac{1}{D_0 - D_1}\ln\left(\frac{I_7}{I_1}\right)$$

Figure 4.7. Method for analytically determining the dose attenuation coefficient (not to scale)

A simpler, more concise alternative for this calculation eliminates the regions of air and the associated intensities I_3, I_5, and I_7. The dose attenuation coefficient associated with air is sufficiently small such that it is negligible for this experiment, and the distances between the layers of the M2/M3 BFV's armor are sufficiently small such that the decrease in intensity as prescribed by Newton's inverse-square law is also insignificant. A more succinct calculation for the intensity and subsequent dose attenuation coefficient are given below.

$$I = I_0 \frac{{D_0}^2}{{D_1}^2} e^{-[2\cdot(\mu_{steel}\ell_{steel})+(\mu_{Al5083}\ell_{Al5083})]} \quad \textbf{(4.2)}$$

$$\mu_{wall} = -\frac{1}{D_0 - D_1} \ln\left(\frac{I}{I_0}\right) \quad \textbf{(4.3)}$$

Table 4.10. Theoretical Linear Attenuation Coefficients[†] (Buyuk 1344; Zafer 180002-3)

	^{60}Co 1.253 MeV	^{137}Cs[†] 0.662 MeV	^{226}Ra[‡] 0.190 MeV
μ_{air}	6.69×10^{-5}	9.11×10^{-5}	1.48×10^{-4}
μ_{Al5083}	8.56×10^{-2}	2.02×10^{-2}	3.41×10^{-1}
μ_{steel}[§]	4.34×10^{-1}	5.69×10^{-1}	1.20

[†] Linear attenuation coefficients for cast iron were not used; the beam was not aimed through the engine.
[‡] Exponential interpolation was used to determine the linear attenuation coefficient for nuclides whose gamma photon energy and associated linear attenuation coefficient fell between two specified, NIST XCOM theoretical values.
[§] The linear attenuation coefficient chosen for high hardness steel was that of a boron steel, 27M12C5B, for its similar chemical composition.

Table 4.11. Analytical Dose Attenuation Coefficients

Position	μ		
	^{60}Co	^{137}Cs	^{226}Ra
A2	0.00288	0.00461	0.00890
A3	0.00289	0.00462	0.00892
B4	0.00287	0.00459	0.00885
C4	0.00277	0.00442	0.00854
D4	0.00292	0.00468	0.00903
E4	0.00297	0.00475	0.00917
F3	0.00240	0.00384	0.00741
F2	0.00245	0.00391	0.00755
E1	0.02951	0.04735	0.09168
D1	0.02521	0.04046	0.07833
C1	0.01615	0.02592	0.05017
B1	0.01652	0.02650	0.05129

Determining the dose attenuation coefficient analytically provides somewhat improved results. For all positions, ^{60}Co has the smallest dose attenuation coefficient. Likewise, ^{226}Ra consistently has the largest. However, confidence in these values remains low considering the sources' proximity to the detector during background measurements, the unconfirmed construct the M2/M3 BFV, and use of dose attenuation coefficients for a similar but not exact steel alloy. Furthermore, the analytical results presented here have not accounted for the buildup factor, a parameter of particular importance for poorly collimated, broad beams and thick shields. In such cases, photons experience considerably greater scatter than in the ideal case of a perfectly collimated beam with a thin slab geometry. The buildup factor, a value greater than 1, accounts for those photons which have undergone Compton scattering and have influenced secondary radiations. Additionally, for sources such as ^{60}Co that emit photons whose energy is 1.02 MeV or greater, pair production effects must also be considered ("Pair production"). Thus, a more appropriate equation to use for the calculations presented here is

$$I = I_0 B\, e^{-\mu \ell} \quad \textbf{(4.2)}$$

where *B* is the buildup factor.

4.4 Improvements to the Experiment Design

This experiment's greatest value lies in its ability to serve as a foundation for future work. The design is rudimentary and several procedural flaws exist in part due to minimal resources being shared between two research groups with different goals. Regrettably, the M2/M3 BFV was only available for a very limited amount of time, this particular project was not the priority, and there was some difficulty in determining the best way to collect data in attempting to mesh two research agendas.

4.4.1 Detector and Source Selection

While the AN/VDR-2 is certainly capable of measuring gamma radiation, a survey instrument of this sort is not the most appropriate detector for use in this experiment. A more viable option would be the cost-effective, widely popular, thallium-doped sodium iodide (NaI(Tl)) crystal scintillator. Since their late 1940s debut, NaI(Tl) scintillators have come to be the industry standard for gamma photon applications (Knoll 239).

A scintillator, such as the NaI(Tl) scintillator, detects radiation when the particle of interest strikes its crystal and causes light photon emission. The light photon strikes the photocathode causing a photoelectron to be emitted into a photomultiplier tube (PMT) where a series of dynodes cause a cascade of electrons to be emitted. These electrons arrive at the anode and send a signal to the measuring device that generates outputs for the user ("What are scintillators?").

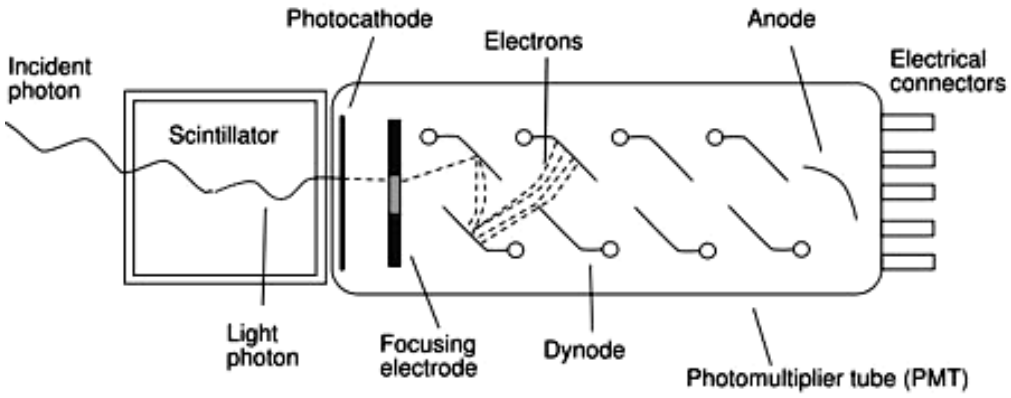

Figure 4.8. Schematic of a typical scintillator ("What are scintillators?")

As for the AN/VDR-2, one could more appropriately employ it as the subject of its own test to determine the level of accuracy of its built-in attenuation factors. That is, once the true attenuation characteristics of the M2/M3 BFV are determined, one could compare the AN/VDR-2's attenuation factors to the newly established attenuation factors. Vehicles such as the M2/M3 BFV have certainly been upgraded since their initial fielding in the 1980s, and as such, it is feasible that attenuation factors currently in use are no longer as accurate as they once were.

The sources chosen for this experiment had activities of 10 mCi and 82.3 mCi. Given the level of shielding provided by M2/M3 BFV's armor, a source with greater activity, perhaps as a high as 1 Ci, is desirable. Concerning the nuclides chosen, the most logical choices for sources are those that, as a group, cover a relatively large energy range and those that are most likely to be found in considerable quantities following the

detonation of a nuclear weapon. The nuclides used in this experiment, ^{60}Co, ^{137}Cs, and ^{226}Ra, indeed, cover a reasonable range of energies. However, ^{137}Cs is the only nuclide that is produced in large enough quantities and has been deemed significant by the DoD considering its internal dose effects following nuclear weapons detonation. Other significant nuclides include carbon-14 (^{14}C), strontium-89 (^{89}Sr), strontium-90 (^{90}Sr), and iodine-131 (^{131}I) (*Estimates and Evaluation of Fallout in the United States*). Of these, the only suitable candidate for use as a gamma emitter is ^{131}I which has an average gamma photon energy of 0.407 MeV and could be included as a source provided the appropriate logistical considerations were taken into account given its 8-day half-life.

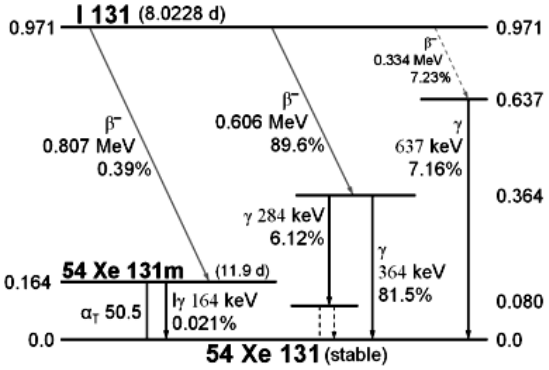

Figure 4.9. Decay scheme for ^{131}I ("I 131 Decay Scheme")

4.4.2 Procedural Considerations

Several procedural missteps were noted during this experiment. As previously stated, the AN/VDR-2's attenuation settings were not verified to be set to 1.0 prior to the start of the experiment. In effect, one cannot consider the measurements taken during the course of the experiment to be accurate and true. Additionally, the measurements were taken with both the rear ramp lowered and the driver's hatch raised. Leaving the vehicle

in this configuration will potentially allow photons to reach the detector without passing through any portion of the M2/M3 BFV's walls especially when the source is poorly collimated. Raising the rear ramp to its closed position and lowering all hatches to their closed positions is the ideal configuration for this experiment.

Also as previously discussed, the sources were allowed to remain in considerably close proximity to the vehicle while taking background radiation measurements. A more preferable technique for measuring background radiation includes allowing the sources to remain in their shielded storage or shipping containers at a distance of no less than 10 m from the vehicle.

The exact angle of the source to the detector was not measured or recorded during the experiment; the distance from the source to the detector is, therefore, an estimate and increases the uncertainty associated with calculating the experimental and analytical dose attenuation coefficients. It stands to reason that future work should include exact measurements rather than estimates.

The sources in this experiment were only roughly collimated using lead bricks. In attenuation coefficient studies, it is a far better technique to use a narrow beam collimator to attain the best beam quality possible.

Measurements for each source were only taken along the front, rear, and sides of the M2/M3 BFV: no measurements were taken at the corners which correspond to positions A1, A4, E1, and E4. At the position beneath the vehicle, Z0, the only measurement taken was the measurement taken with the AN/VDR-2 internally installed in the vehicle: the corresponding measurement with the detector located outside of the

vehicle in an identical position was not taken, rendering the position unusable in experimentally determining the attenuation characteristics of the undercarriage of the M2/M3 BFV. The Z0 position is of notable interest; in a radiation field resulting from the fallout of a nuclear weapon detonation, one expects an overwhelming amount of groundshine to spur photon interactions with the undercarriage of the vehicle.

In allowing the pulse rate to stabilize, 180 s elapsed for all three sources while the AN/VDR-2 was internally installed in the vehicle. However, just 60 s was allowed to elapse when allowing the pulse rate to stabilize for ^{60}Co and ^{226}Ra when the detector was placed outside of the M2/M3 BFV in an identical position, and just 30 s was allowed to elapse for ^{137}Cs. In an effort not to introduce additional and unnecessary variables, the time allowed for the pulse rate to stabilize should be held constant.

None of the measurements taken throughout the experiment were taken in duplicate or, more preferably, in triplicate. This, too, increases the amount of uncertainty associated with the experiment and renders statistical analysis and subsequent results validation difficult if not impossible.

4.4.3 Experiment Design Considerations

One of the most considerable deficiencies in the overall design of the experiment is that measurements were only taken with the source placed at distances of 100 cm from the wall of the vehicle. A more thorough dose attenuation study could include a setup that takes measurements with a properly collimated source placed at the same height as the detector and at equal distances from the detector (rather than the wall of the vehicle)

at 100 cm intervals in five concentric rings as depicted in Figure 4.8. This would allow for 40 source positions around the vehicle and one additional position with the collimated source placed beneath the vehicle directly under the detector for a total for 41 positions.

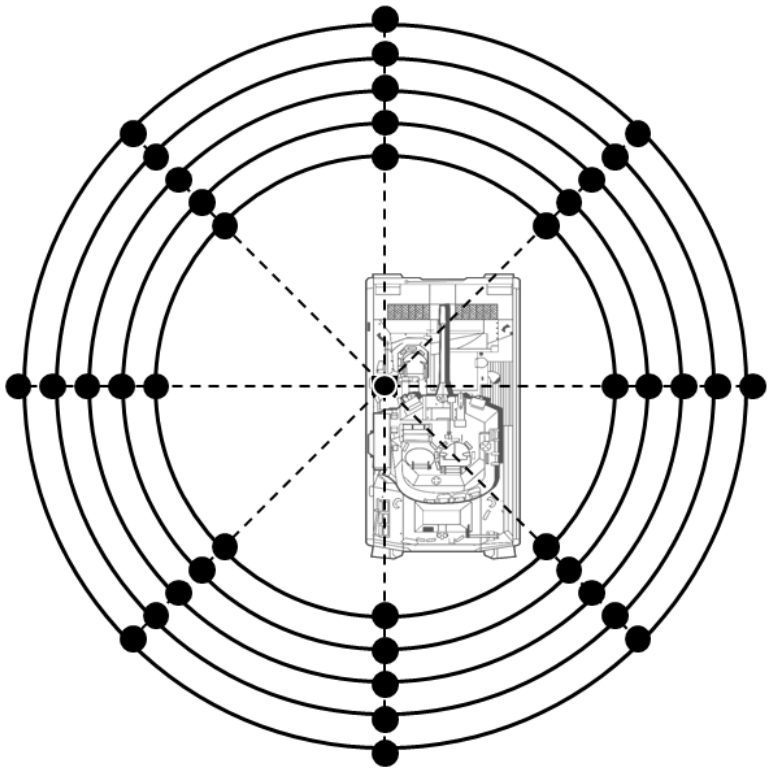

Figure 4.10. Experiment design for an improved dose attenuation study (not to scale)

With regard to the orientation of the detector, ensuring that the detector face was kept normal to the collimated beam would further ensure more reliable results. During the Fort Benning experiments, the AN/VDR-2 was installed with the face normal to the side walls of the M2/M3 BFV. However, as the source was positioned around the vehicle, the detector was not repositioned, subsequently decreasing the surface area of the detector face that was directly in-line with the beam. In a case such as this where the beam was not well collimated, one can reasonably postulate that the effects of not repositioning the detector were somewhat diminished with the broadening of the beam.

Considering the manner in which absorbed dose rates at the detector varied based on the position of the source, one could consider fixing dosimeters at various locations inside of the M2/M3 BFV to better characterize the radiological environment inside of the vehicle as opposed to at the detector. Furthermore, these measurements in conjunction with the measurements from the detector placed at the prescribed installation position could provide some insight as to how the vehicle's internal structures affect the amount of radiation that actually reaches the detector.

If the interest was to observe how detector response varies with the detector internally installed in a vehicle versus with the detector placed in an identical position outside of the vehicle in a radiation field, one could simulate at radiation field using four uncollimated sources 90° apart from each other placed at ground level at equal distances from the detector at 100 cm-intervals in five concentric rings. Then, the sources could be rotated by 45° to study the detector response with the simulated radiation field in an alternate configuration. This setup would allow for 10 source positions around the vehicle to observe how detector response varies with a radiation field that grows weaker as the radius around the detector increases.

(continued on next page)

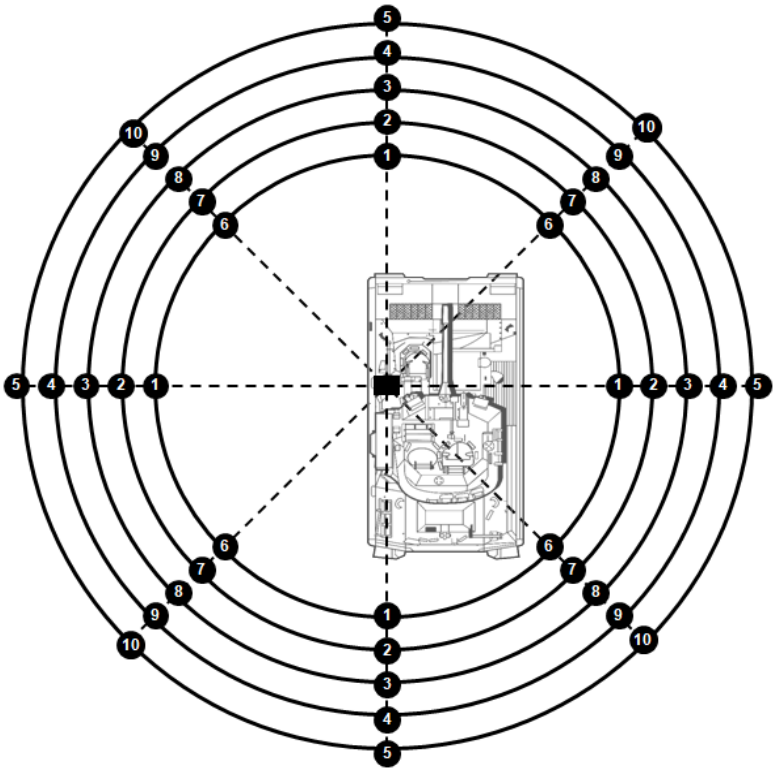

Figure 4.11. Experiment design for a detector response study conducted in a radiation field (not to scale)

Used as a means to predict the outcome of a real-world experiment, computational modeling is a viable tool that can and should be used to guide and validate future experiment design: "[computational modeling] can expedite research by allowing scientists to conduct thousands of simulated experiments by computer in order to identify the actual physical experiments that are most likely to help the researcher find the solution to the problem being studied" ("Computational Modeling").

CHAPTER 5. COMPUTATIONAL METHODOLOGY AND PROCEDURES

As previously discussed, computational modeling is a powerful tool that can aid in experiment design. However, in this case, computational modeling has been useful in attempting to collect better, more reliable data with decreased impacts from human error and otherwise poor judgment. For the purposes of comparison, the experiment design has not been changed.

The MCNP Transport Code version 6.1.0 (released July 2013) was used for computational modeling of the experiment. All simulations were run on a Hewlett-Packard ENVY Laptop Computer - 17t with 64-bit Microsoft Windows 10 operating system, 16 GB RAM, and an Intel® Core™ i7-855OU four-core processor with 1.85 GHz (up to 4.00 GHz) frequency.

The input files for the simulations include a very rough approximation of the M2/M3 BFV's geometry. Only the turret, hull, undercarriage armor plate, and engine block have been modeled, as these elements are the most prominent features that would contribute to gamma attenuation. All of these elements have been modeled as rectangular prisms with dimensions that approximate those of the element concerned. The turret and the hull are represented by six, nested cells which approximate the vehicle's armor. From the innermost to outermost, the cells' materials are air, aluminum 5083, air, high hardness steel, air, and high hardness steel. The undercarriage armor plate is modeled as high hardness steel, and the engine block is modeled as cast iron. The M2/M3 BFV's tracks have not been modeled, which leads to an overall vehicle height reduction of 46 cm. The source and detector heights used in the simulation have been adjusted accordingly.

Other dimensions used for modeling the M2/M3 BFV and detector placement were those recorded during the Fort Benning experiments (see Table 3.1). Additional measurements for the hull and turret which include the height for both elements and the length and width for the hull were adapted from the M2/M3 BFV's technical drawings and specifications. Dimensions for the undercarriage armor plate was adapted from the open source reports on the vehicle's construct, and dimensions for the engine block were adapted from estimates made based on technical drawings. All areas around the M2/M3 BFV were modeled as air. In the case where the detector was placed outside of the vehicle in an identical position, all elements of the M2/M3 BFV were also modeled as air.

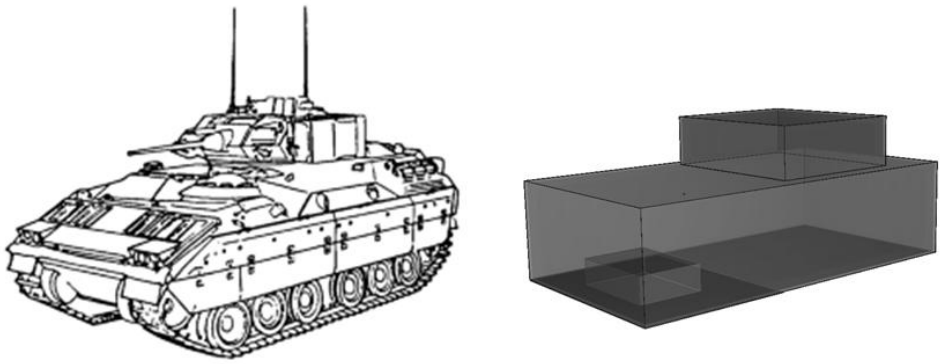

Figure 5.1. Side-by-side comparison of the M2/M3 BFV's technical drawing and MCNP model used for this simulation (*TM 9-2350-252-10-1*).

The detector probe's face was modeled as a cylindrical cell with height 0.22 cm and radius 1.53 cm and was placed in a position and orientation comparable to that of the AN/VDR-2's DT-616 probe face. The detector probe's face material was set to air, as the tallies used for this experiment captured measurements for fluence. As such, the

composition of the detector face is considerably more trivial than in taking measurements for energy deposited over a cell.

Sources used in the experiment were modeled as point sources with discrete energy photons monodirectionally aimed at the detector cell.

Several tallies were considered for use in determining the dose attenuation coefficient. Those considered included the F4 tally, which provides the average flux in a cell, and the F5 tally, which provides the flux at a point or a ring. Each of the tallies was modified by two, built-in dose energy and dose function cards (flux-to-dose rate conversion factors)—the International Commission on Radiological Protection (ICRP) 21 1971 conversion factors for photons and the American National Standards Institute/American Nuclear Society (ANSI/ANS) 6.1.1 -1977 conversion factors for photons. A third set of conversion factors representing the ICRP 74 1996 conversion factors for photons was entered manually ("MCNP"). The quality factor parameter for the conversions was set to 1 given that gamma photons were the particle of interest (10 CFR 20.1004).

In addition to modeling the Fort Benning experiments, one additional experiment was modeled. The sources were changed from point sources monodirectionally aimed at the detector cell to a broad, monodirectional disk sources centered under the M2/M3 BFV to simulate a radiation field.

CHAPTER 6. COMPUTATIONAL DATA ANALYSIS AND RESULTS

6.1 The Absorbed Dose Rate

Similarities and dissimilarities between the experimental and computational data are not immediately obvious and require some treatment before a comparison can be made: data outputs from the MCNP tallies were given in units of rem/h per photon for tallies modified by the built-in flux-to-dose rate conversion factors, while tallies modified by the user-specified ICRP 74 1996 conversion factors were given in units of pSv/cm^2 per second (Hertel). As such, all data outputs were converted to absorbed dose rates of μGy/h, the units used during the Fort Benning experiment. Data from the F5 tallies was not considered: variances associated with these tallies were exceptionally high, and tallies of type 5 are "susceptible to unreliable results if used improperly" (Pelowitz 3-181). Thus, only data from the F4 tallies has been analyzed.

$$\frac{1\ rem}{h} = \frac{10\ mGy}{h} = \frac{10{,}000\ \mu Gy}{h}$$

Conversion Factor – rem/h to μGy/h
(Taken from *Gamma Radiation Dose Rate Conversions)*

$$A\ \frac{\cancel{rem}}{h \cdot \cancel{photon}} \cdot \frac{10{,}000\ \mu Gy}{\cancel{rem}} \cdot B\ \frac{\cancel{photons}}{\cancel{cm^2}} \cdot C\ \cancel{cm^2} = X\ \frac{\mu Gy}{h}$$

A rem/(h · photon) is the flux-to-dose tally provided by MCNP for the detector cell
B photons/cm^2 is the is the fluence tally provided by MCNP for the detector cell
C cm^2 is the detector cell's probe face surface area
X μGy/hr is the converted data output

Figure 6.1. Conversion calculation for rem/h to μGy/h.

$$\frac{1\ pSv}{cm^2} = \frac{1\ pGy}{cm^2} = \frac{0.000001\ \mu Gy}{cm^2}$$

Conversion Factor – rem/h to µGy/h
(Taken from *Gamma Radiation Dose Rate Conversions)*

$$A\ \frac{\cancel{pSv}}{\cancel{cm^2 \cdot s}} \cdot \frac{0.000001\ \mu Gy}{\cancel{pSv}} \cdot \frac{3600\ \cancel{s}}{h} \cdot B\ \cancel{cm^2} = X\ \frac{\mu Gy}{h}$$

A pSv/(cm^2 · s) is the flux-to-dose tally provided by MCNP for the detector cell
B cm^2 is the detector cell's probe face surface area
X µGy/hr is the converted data output

Figure 6.2. Conversion calculation for pSv/cm^2 · s to µGy/h.

(continued on next page)

Table 6.1. Computational Absorbed Dose Data for ^{60}Co – Detector Internally Installed in the M2/M3 BFV

Position	Experimental Net Absorbed Dose Rate (μGy/h)	Computational Absorbed Dose Rates (μGy/h)		
		ICRP 21 1974	ANSI/ANS 6.1.1 1977	ICRP 74 1996
A2	1.02	1.04×10^{-2}	1.13×10^{-2}	1.06×10^{-2}
A3	2.53	1.56×10^{-3}	1.70×10^{-3}	1.59×10^{-3}
B4	0.62	4.84×10^{-4}	5.26×10^{-4}	4.94×10^{-4}
C4	0.37	4.81×10^{-4}	5.23×10^{-4}	4.91×10^{-4}
D4	0.24	4.83×10^{-4}	5.25×10^{-4}	4.93×10^{-4}
E4	-0.10	4.80×10^{-4}	5.21×10^{-4}	4.90×10^{-4}
F3	-0.09	2.00×10^{-3}	2.17×10^{-3}	2.04×10^{-3}
F2	0.12	2.79×10^{-2}	3.02×10^{-2}	2.84×10^{-2}
E1	-0.24	3.02×10^{-4}	3.28×10^{-4}	3.08×10^{-4}
D1	2.88	5.00×10^{-4}	5.43×10^{-4}	5.10×10^{-4}
C1	6.09	5.07×10^{-4}	5.50×10^{-4}	5.17×10^{-4}
B1	0.63	3.82×10^{-4}	4.14×10^{-4}	3.89×10^{-4}

Table 6.2. Computational Absorbed Dose Data for ^{60}Co – Detector Located Outside of the M2/M3 BFV in an Identical Position

Position	Experimental Net Absorbed Dose Rate (μGy/h)	Computational Absorbed Dose Rates (μGy/h)		
		ICRP 21 1974	ANSI/ANS 6.1.1 1977	ICRP 74 1996
A2	21.09	1.64×10^{-1}	1.78×10^{-1}	1.64×10^{-1}
A3	15.50	1.17×10^{-2}	1.27×10^{-2}	1.20×10^{-2}
B4	12.72	3.63×10^{-3}	3.94×10^{-3}	3.70×10^{-3}
C4	13.10	2.85×10^{-3}	3.09×10^{-3}	2.90×10^{-3}
D4	8.82	2.99×10^{-3}	3.25×10^{-3}	3.05×10^{-3}
E4	5.02	4.07×10^{-3}	4.42×10^{-3}	4.15×10^{-3}
F3	2.43	1.42×10^{-2}	1.54×10^{-2}	1.45×10^{-2}
F2	1.90	1.63×10^{-1}	1.77×10^{-1}	1.66×10^{-1}
E1	4.46	1.29×10^{-2}	1.40×10^{-2}	1.31×10^{-2}
D1	10.39	4.54×10^{-3}	4.92×10^{-3}	4.62×10^{-3}
C1	24.81	3.39×10^{-3}	3.68×10^{-3}	3.46×10^{-3}
B1	26.21	9.51×10^{-3}	1.03×10^{-2}	9.70×10^{-3}

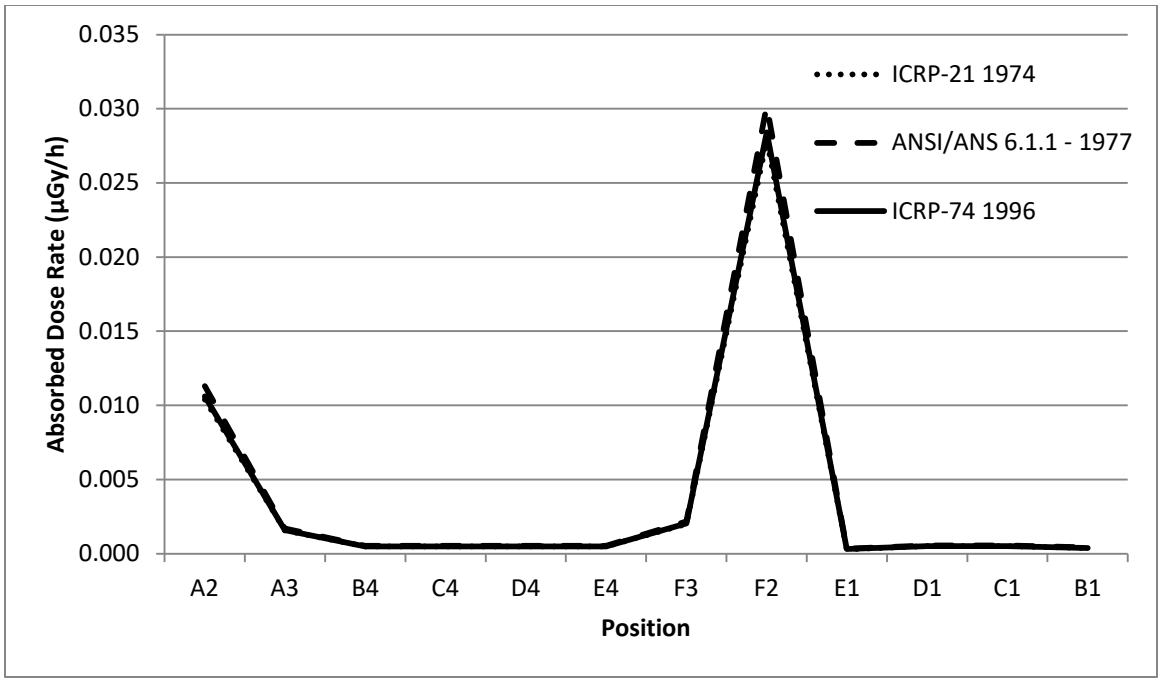

Figure 6.3. Plot of Position vs. Computational Absorbed Dose Rate for ^{60}Co – Detector Internally Installed in the M2/M3 BFV

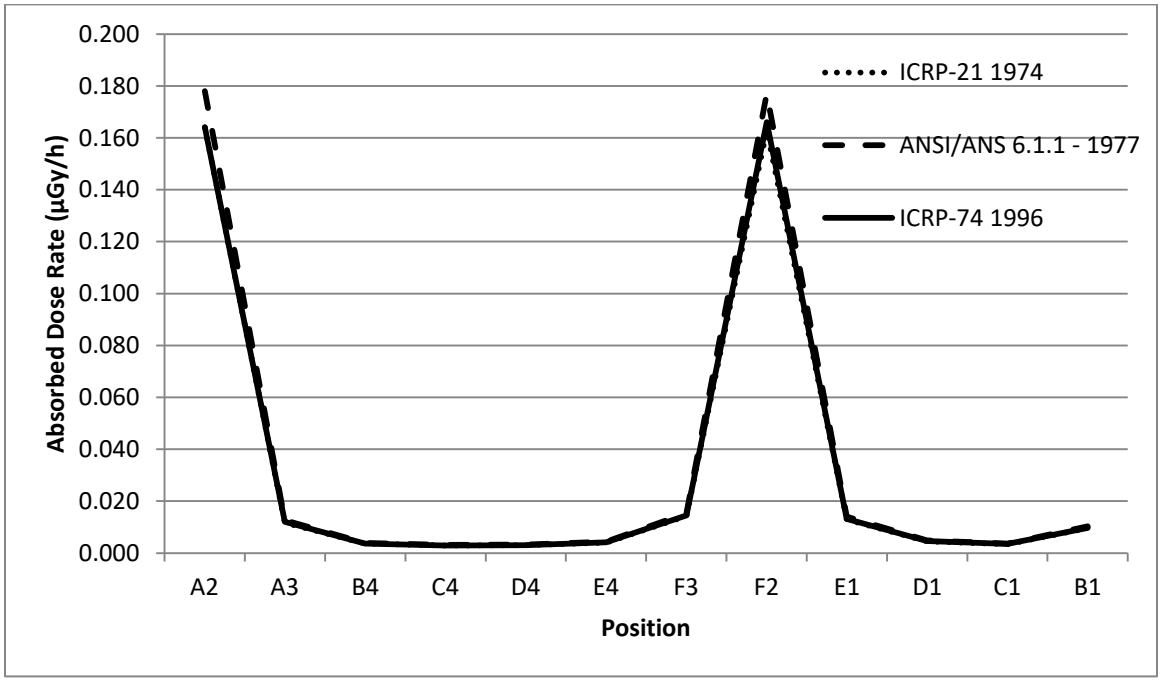

Figure 6.4. Plot of Position vs. Computational Absorbed Dose Rate for ^{60}Co – Detector Located Outside of the M2/M3 BFV in an Identical Position

Table 6.3. Computational Absorbed Dose Data for ^{137}Cs – Detector Internally Installed in the M2/M3 BFV

Position	Experimental Net Absorbed Dose Rate (μGy/h)	Computational Absorbed Dose Rates (μGy/h)		
		ICRP 21 1974	ANSI/ANS 6.1.1 1977	ICRP 74 1996
A2	-0.14	8.36×10^{-3}	9.74×10^{-3}	8.97×10^{-3}
A3	-0.06	4.26×10^{-4}	4.97×10^{-4}	4.58×10^{-4}
B4	0.05	1.31×10^{-4}	1.53×10^{-4}	1.41×10^{-4}
C4	0.16	1.43×10^{-4}	1.67×10^{-4}	1.54×10^{-4}
D4	0.51	1.41×10^{-4}	1.64×10^{-4}	1.51×10^{-4}
E4	0.25	1.24×10^{-4}	1.45×10^{-4}	1.34×10^{-4}
F3	2.71	5.51×10^{-4}	6.46×10^{-4}	5.95×10^{-4}
F2	1.97	8.29×10^{-3}	9.96×10^{-3}	8.90×10^{-3}
E1	0.30	4.35×10^{-5}	5.07×10^{-5}	4.67×10^{-5}
D1	2.26	1.29×10^{-4}	1.50×10^{-4}	1.38×10^{-4}
C1	8.02	1.46×10^{-4}	1.70×10^{-4}	1.57×10^{-4}
B1	1.36	6.73×10^{-5}	7.84×10^{-5}	7.22×10^{-5}

Table 6.4. Computational Absorbed Dose Data for ^{137}Cs – Detector Located Outside of the M2/M3 BFV in an Identical Position

Position	Experimental Net Absorbed Dose Rate (μGy/h)	Computational Absorbed Dose Rates (μGy/h)		
		ICRP 21 1974	ANSI/ANS 6.1.1 1977	ICRP 74 1996
A2	36.77	9.40×10^{-2}	1.10×10^{-1}	1.01×10^{-1}
A3	29.31	6.71×10^{-3}	7.82×10^{-3}	7.20×10^{-3}
B4	23.51	2.08×10^{-3}	2.42×10^{-3}	2.23×10^{-3}
C4	24.20	1.63×10^{-3}	1.90×10^{-3}	1.75×10^{-3}
D4	14.98	1.71×10^{-3}	2.00×10^{-3}	1.84×10^{-3}
E4	8.71	2.32×10^{-3}	2.70×10^{-3}	2.49×10^{-3}
F3	2.97	8.10×10^{-3}	9.44×10^{-3}	8.69×10^{-3}
F2	2.79	9.30×10^{-2}	1.08×10^{-1}	9.99×10^{-2}
E1	6.57	7.40×10^{-3}	8.62×10^{-3}	7.94×10^{-3}
D1	47.62	2.62×10^{-3}	3.03×10^{-3}	2.82×10^{-3}
C1	47.60	1.96×10^{-3}	2.29×10^{-3}	2.11×10^{-3}
B1	49.01	5.48×10^{-3}	6.39×10^{-3}	5.88×10^{-3}

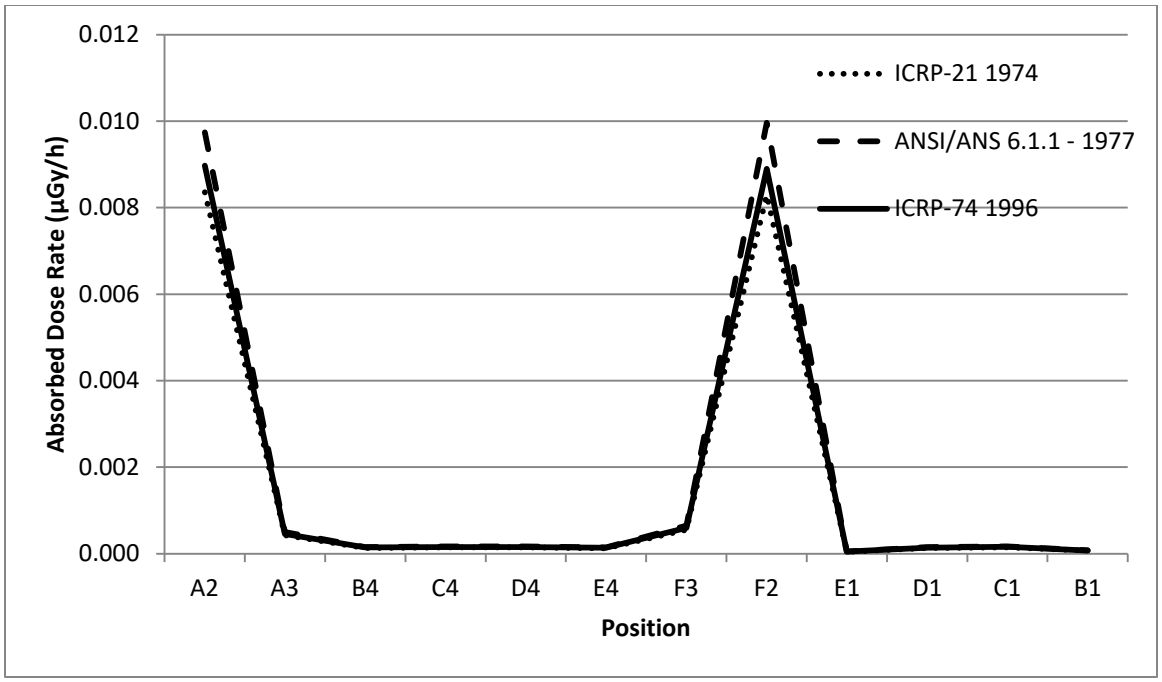

Figure 6.5. Plot of Position vs. Computational Absorbed Dose Rate for ^{137}Cs – Detector Internally Installed in the M2/M3 BFV

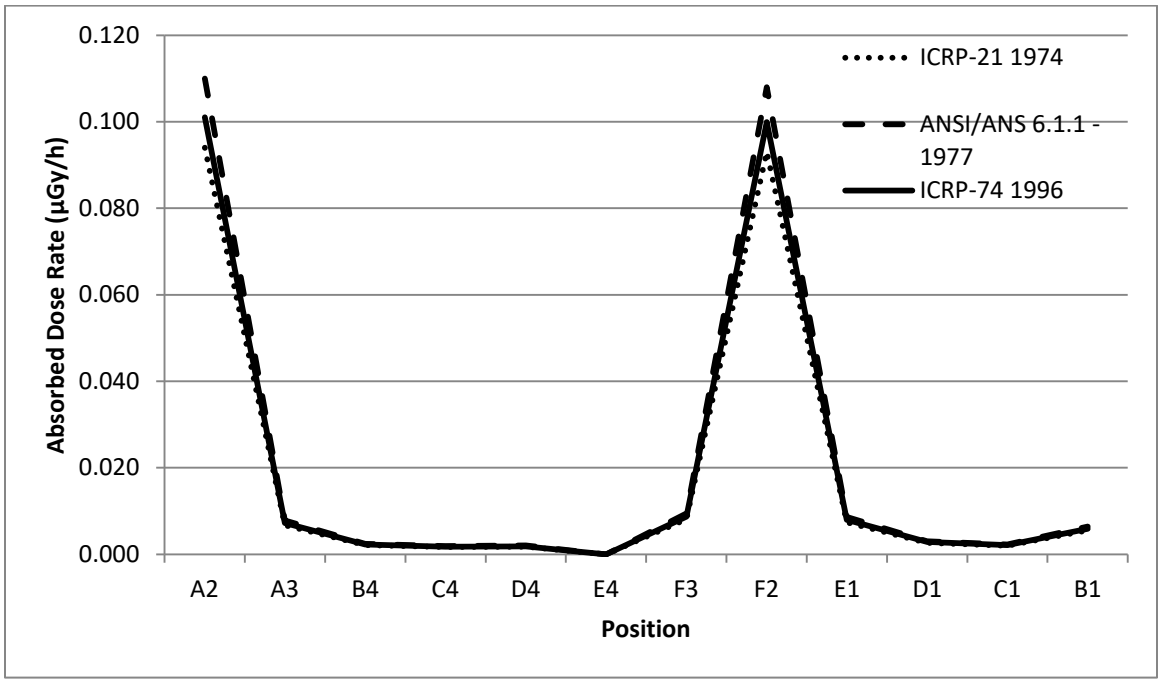

Figure 6.6. Plot of Position vs. Computational Absorbed Dose Rate for ^{137}Cs – Detector Located Outside of the M2/M3 BFV in an Identical Position

Table 6.5. Computational Absorbed Dose Data for ^{226}Ra – Detector Internally Installed in the M2/M3 BFV

Position	Experimental Net Absorbed Dose Rate (μGy/h)	Computational Absorbed Dose Rates (μGy/h)		
		ICRP 21 1974	ANSI/ANS 6.1.1 1977	ICRP 74 1996
A2	0.17	7.25×10^{-15}	1.27×10^{-15}	1.01×10^{-14}
A3	1.99	1.05×10^{-14}	1.89×10^{-14}	1.48×10^{-14}
B4	0.04	2.33×10^{-6}	3.45×10^{-6}	2.94×10^{-6}
C4	0.30	3.48×10^{-6}	5.14×10^{-6}	4.38×10^{-6}
D4	0.39	3.23×10^{-6}	4.77×10^{-6}	4.06×10^{-6}
E4	0.04	1.89×10^{-6}	2.79×10^{-6}	2.37×10^{-6}
F3	0.44	1.06×10^{-5}	1.56×10^{-5}	1.33×10^{-5}
F2	0.01	2.04×10^{-4}	3.01×10^{-4}	2.57×10^{-4}
E1	0.13	8.28×10^{-8}	1.22×10^{-7}	1.04×10^{-7}
D1	2.15	1.88×10^{-6}	2.78×10^{-6}	2.37×10^{-6}
C1	4.73	3.19×10^{-6}	4.71×10^{-6}	4.01×10^{-6}
B1	0.99	2.59×10^{-7}	3.82×10^{-7}	3.26×10^{-7}

Table 6.6. Computational Absorbed Dose Data for ^{226}Ra – Detector Located Outside of the M2/M3 BFV in an Identical Position

Position	Experimental Net Absorbed Dose Rate (μGy/h)	Computational Absorbed Dose Rates (μGy/h)		
		ICRP 21 1974	ANSI/ANS 6.1.1 1977	ICRP 74 1996
A2	13.11	2.29×10^{-2}	3.38×10^{-2}	2.88×10^{-2}
A3	10.63	1.62×10^{-3}	2.40×10^{-3}	2.05×10^{-3}
B4	9.22	5.02×10^{-4}	7.42×10^{-4}	6.32×10^{-4}
C4	8.87	3.96×10^{-4}	5.86×10^{-4}	4.99×10^{-4}
D4	5.61	4.16×10^{-4}	6.15×10^{-4}	5.24×10^{-4}
E4	3.25	5.60×10^{-4}	8.27×10^{-4}	7.05×10^{-4}
F3	1.76	1.95×10^{-3}	2.88×10^{-3}	2.46×10^{-3}
F2	1.30	2.25×10^{-2}	3.33×10^{-2}	2.84×10^{-2}
E1	3.05	1.82×10^{-3}	2.69×10^{-3}	2.29×10^{-3}
D1	7.39	6.54×10^{-4}	9.66×10^{-4}	8.24×10^{-4}
C1	15.62	4.91×10^{-4}	7.25×10^{-4}	6.18×10^{-4}
B1	17.34	1.35×10^{-3}	2.00×10^{-3}	1.70×10^{-3}

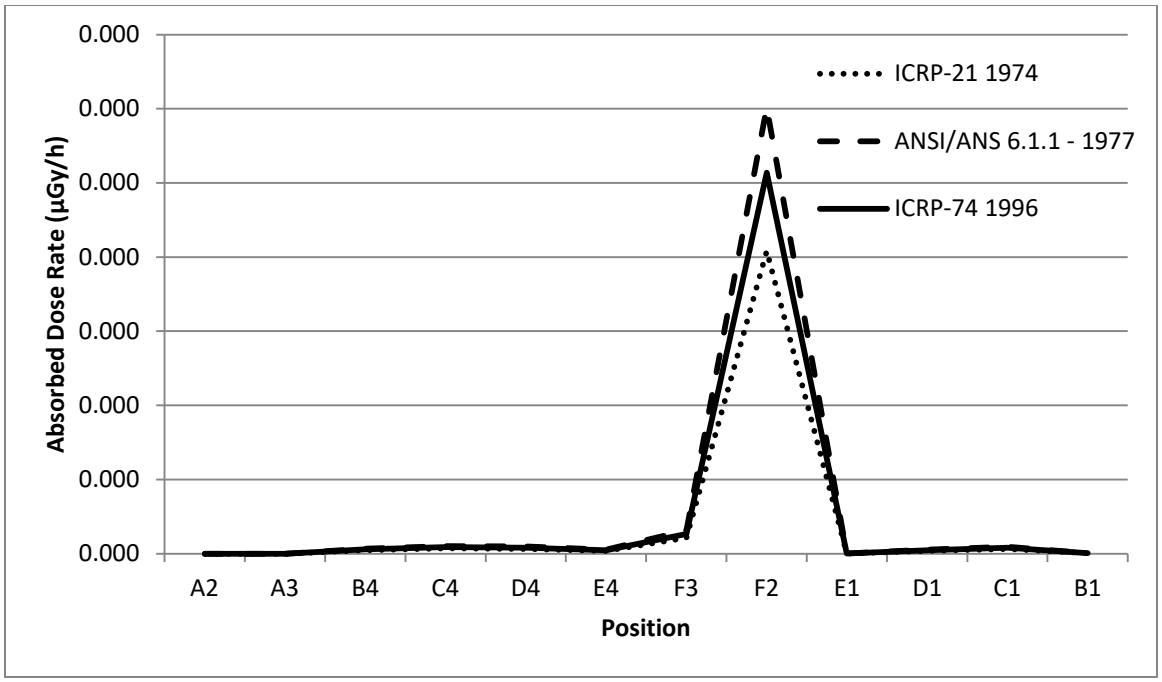

Figure 6.7. Plot of Position vs. Computational Absorbed Dose Rate for ^{226}Ra – Detector Internally Installed in the M2/M3 BFV

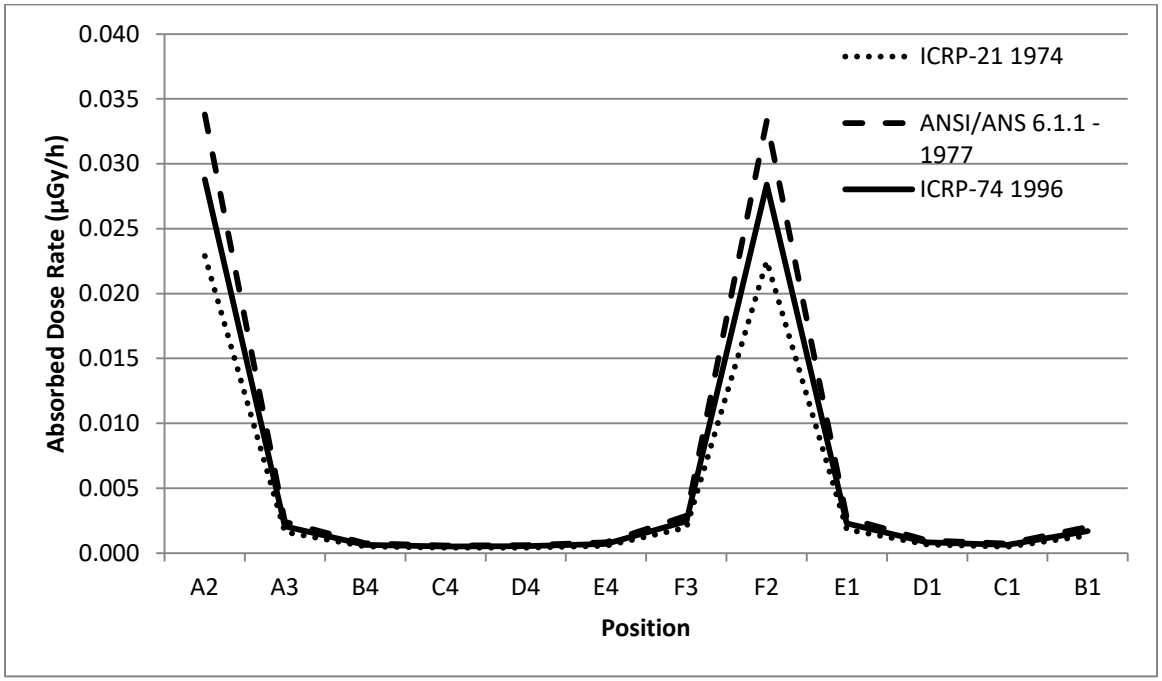

Figure 6.8. Plot of Position vs. Computational Absorbed Dose Rate for ^{229}Ra – Detector Located Outside of the M2/M3 BFV in an Identical Position

Upon treating the data, it becomes immediately obvious that the MCNP model has generated absorbed dose rate measurements significantly lower than the dose rates measured with the AN/VDR-2. The computational absorbed dose rates are 10^{-2} to 10^{-14} times smaller than the experimental absorbed dose rates with most varying by a factor between 10^{-2} and 10^{-4}. However, comparison of the experimental and computational values is not altogether meaningful considering that the AN/VDR-2 attenuation factor settings were not verified to be 1.0 and the use of lead bricks as a collimator and, subsequently, the photons that may have penetrated the lead bricks to go on to reach the detector.

In reviewing the plots of position versus computational absorbed dose rates, one finds that measurements associated with the position C1 are not the largest absorbed dose rates despite the detector's proximity to the source. In the computational model, the source placed position A2 usually generates of the highest absorbed dose rate measurements, and in all cases, the source being placed at position F2 generates comparable dose rates. Nevertheless, one unsurprisingly notices that the computational plots agree with each other quite well and even more so than the experimental plots. Unlike the experimental plots, the computational plots generally follow the same trends when the detector is internally installed in the M2/M3 BFV and when the detector is placed outside of the M2/M3 BFV in an identical position.

6.2 Calculating the Computational Dose Attenuation Coefficient

The same method for calculating the dose attenuation coefficient experimentally was used in calculating the dose attenuation coefficient using computational data.

Table 6.7. Computational Dose Attenuation Coefficients for ^{60}Co

Position	ℓ (cm)	μ		
		ICRP 21 1974	ANSI/ANS 6.1.1 1977	ICRP 74 1996
A2	374.11	0.00738	0.00738	0.00738
A3	425.96	0.00473	0.00473	0.00473
B4	436.88	0.00461	0.00461	0.00461
C4	385.26	0.00461	0.00461	0.00461
D4	395.34	0.00461	0.00461	0.00461
E4	463.11	0.00461	0.00461	0.00461
F3	469.87	0.00417	0.00417	0.00417
F2	423.43	0.00417	0.00417	0.00417
E1	298.40	0.01257	0.01257	0.01257
D1	175.70	0.01255	0.01255	0.01255
C1	151.67	0.01253	0.01253	0.01253
B1	255.82	0.01257	0.01257	0.01257

Table 6.8. Computational Dose Attenuation Coefficients for ^{137}Cs

Position	ℓ (cm)	μ		
		ICRP 21 1974	ANSI/ANS 6.1.1 1977	ICRP 74 1996
A2	374.11	0.00647	0.00647	0.00647
A3	425.96	0.00647	0.00647	0.00647
B4	436.88	0.00632	0.00632	0.00632
C4	385.26	0.00632	0.00631	0.00631
D4	395.34	0.00632	0.00632	0.00632
E4	463.11	0.00632	0.00598	0.00598
F3	469.87	0.00571	0.00571	0.00571
F2	423.43	0.00571	0.00571	0.00571
E1	298.40	0.01721	0.01721	0.01721
D1	175.70	0.01716	0.01716	0.01716
C1	151.67	0.01713	0.01713	0.01713
B1	255.82	0.01720	0.01720	0.01720

Table 6.9. Computational Dose Attenuation Coefficients for ^{226}Ra

Position	ℓ (cm)	μ		
		ICRP 21 1974	ANSI/ANS 6.1.1 1977	ICRP 74 1996
A2	374.11	0.07693	0.07648	0.07666
A3	425.96	0.06048	0.06003	0.06022
B4	436.88	0.01229	0.01229	0.01229
C4	385.26	0.01229	0.01229	0.01229
D4	395.34	0.01229	0.01229	0.01229
E4	463.11	0.01229	0.01229	0.01229
F3	469.87	0.01111	0.01111	0.01111
F2	423.43	0.01111	0.01111	0.01111
E1	298.40	0.03350	0.03350	0.03350
D1	175.70	0.03331	0.03331	0.03331
C1	151.67	0.03321	0.03321	0.03321
B1	255.82	0.03347	0.03347	0.03347

As expected, the computational dose attenuation coefficients are notably consistent along the front, rear, and left and right sides of the source for each source. Also as expected, ^{60}Co consistently has the smallest dose attenuation coefficients with ^{226}Ra consistently having the largest with the exception of position A2. These trends were not consistently noted with the experimentally determined dose attenuation coefficients.

6.3 A Comparison of the Experimental, Analytical, and Computational Dose Attenuation Coefficients

Despite unreliable experimentally and analytically determined dose attenuation coefficients, a comparison of the results is presented here for the sake of completeness. For the purposes of this comparison, computational dose attenuation coefficients based on ICRP 21 1974, ANSI/ANS 6.1.1 1977, and ICRP 74 1996 have been averaged. This is generally of no consequence except for dose attenuation coefficients associated with

^{226}Ra at positions A2 and A3 where the values obtained agree very well but are not identical.

A typical detector response curve through a shield is a semilogarithmic plot that illustrates relaxation lengths which increase with penetration distance, or in this case, the variable referred to as length, ℓ (Chilton 152). "Relaxation length, λ, is the thickness of a shielding material that will reduce the intensity of the radiation to 1/e (37%) of its original intensity" and is defined as the inverse of the dose attenuation coefficient μ ("Shielding Radiation").

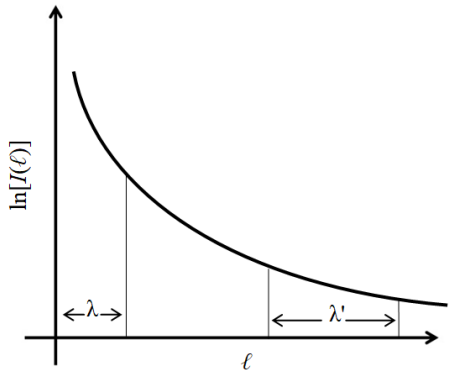

Figure 6.9. Typical detector response curve through a shield (Chilton 152)

In plotting length ℓ versus the computational dose attenuation coefficient μ, the plot does not immediately display the concave shape illustrated above.** However, an exponential line of best fit of the form $y = A\,e^{-bx}$, the same form as the equation for the attenuated intensity *I*, fitted to each curve provides R^2 values of 0.78, 0.70, and 0.30 for ^{60}Co, ^{137}Cs, and ^{226}Ra respectively. This suggests that computational data for ^{60}Co and ^{137}Cs fit the typical detector response model reasonably well.

** Experimental and analytical dose attenuation coefficient data has not been best-fitted due to low confidence in the data obtained.

Table 6.10. Dose Attenuation Coefficients for ^{60}Co

Position	ℓ (cm)	μ			Standard Deviation, σ
		Experimental	Analytical	Computational	
C1	151.67	0.00926	0.01615	0.01253	0.00345
D1	175.70	0.00730	0.02521	0.01255	0.00921
B1	255.82	0.01457	0.01652	0.01257	0.00197
E1	298.40	INSF	0.02951	0.01257	0.01198
A2	374.11	0.00810	0.00288	0.00738	0.00283
C4	385.26	0.00926	0.00277	0.00461	0.00334
D4	395.34	0.00912	0.00292	0.00461	0.00320
F2	423.43	0.00652	0.00245	0.00417	0.00204
A3	425.96	0.00426	0.00289	0.00473	0.00096
B4	436.88	0.00692	0.00287	0.00461	0.00203
E4	463.11	INSF	0.00297	0.00461	0.00116
F3	469.87	INSF	0.00240	0.00417	0.00125

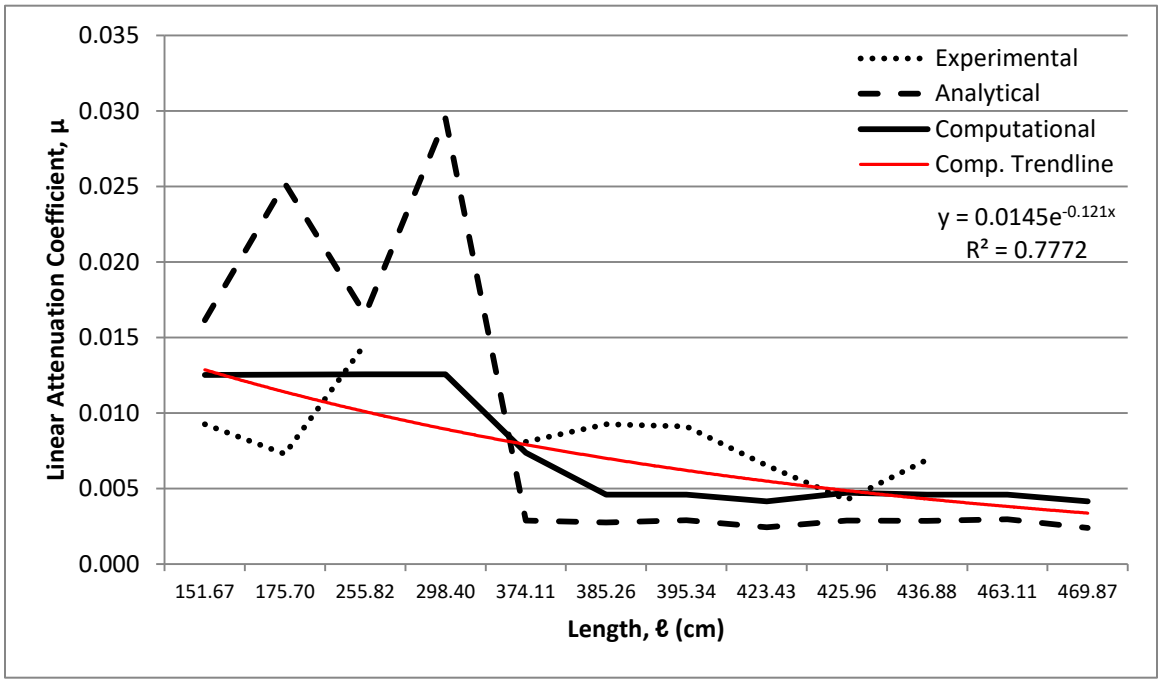

Figure 6.10. Plot of Length vs. Dose Attenuation Coefficient for ^{60}Co

Table 6.11. Dose Attenuation Coefficients for ^{137}Cs

Position	ℓ (cm)	μ			Standard Deviation, σ
		Experimental	Analytical	Computational	
C1	151.67	0.01174	0.02592	0.01713	0.0072
D1	175.70	0.01735	0.04046	0.01716	0.0134
B1	255.82	0.01401	0.02650	0.01720	0.0065
E1	298.40	0.01034	0.04735	0.01721	0.0197
A2	374.11	INSF	0.00461	0.00647	0.0013
C4	385.26	0.01303	0.00442	0.00632	0.0045
D4	395.34	0.00855	0.00468	0.00632	0.0019
F2	423.43	0.00082	0.00391	0.00571	0.0025
A3	425.96	INSF	0.00462	0.00647	0.0013
B4	436.88	0.01408	0.00459	0.00632	0.0051
E4	463.11	0.00767	0.00475	0.00632	0.0015
F3	469.87	0.00019	0.00384	0.00571	0.0028

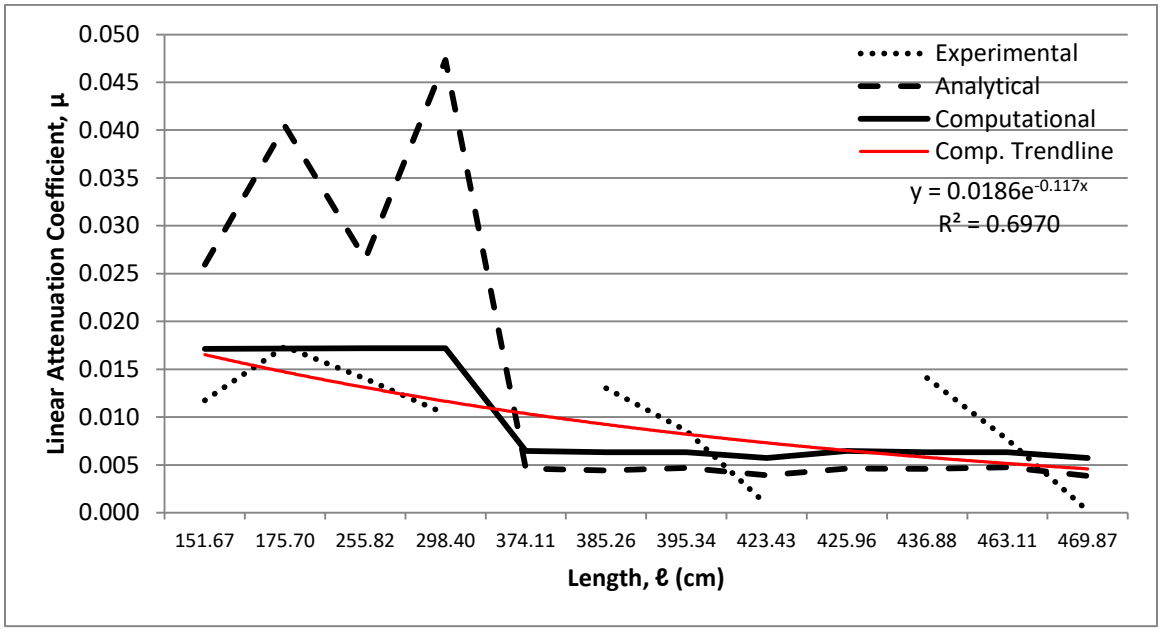

Figure 6.11. Plot of Length vs. Dose Attenuation Coefficient for ^{137}Cs

Table 6.12. Dose Attenuation Coefficients for ^{226}Ra

Position	ℓ (cm)	μ			Standard Deviation, σ
		Experimental	Analytical	Computational	
C1	151.67	0.00788	0.05017	0.03321	0.0213
D1	175.70	0.00703	0.07833	0.03321	0.0361
B1	255.82	0.01119	0.05129	0.03347	0.0201
E1	298.40	0.01057	0.09168	0.03350	0.0418
A2	374.11	0.01162	0.00890	0.07669	0.0384
C4	385.26	0.00879	0.00854	0.01229	0.0021
D4	395.34	0.00674	0.00903	0.01229	0.0028
F2	423.43	0.01150	0.00755	0.01111	0.0022
A3	425.96	0.00393	0.00892	0.06024	0.0312
B4	436.88	0.01245	0.00885	0.01229	0.0020
E4	463.11	0.00950	0.00917	0.01229	0.0017
F3	469.87	0.00295	0.00741	0.01111	0.0041

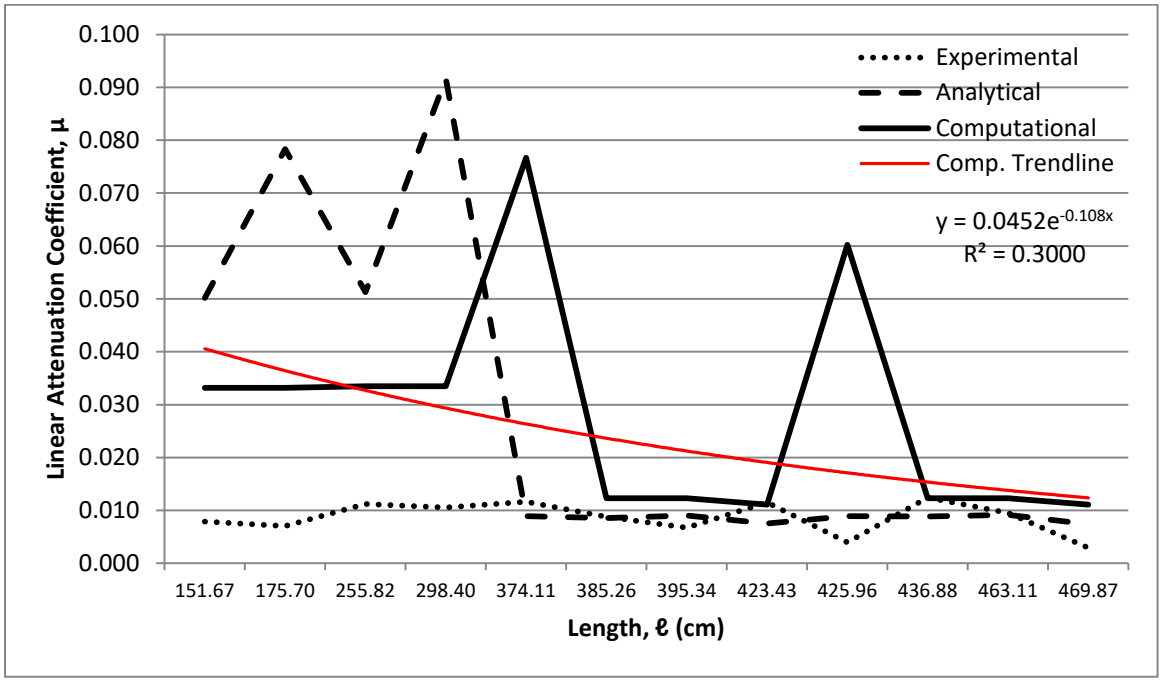

Figure 6.12. Plot of Length vs. Dose Attenuation Coefficient for ^{226}Ra

6.4 Protection Factor

Protection factor (also known as "transmission factor") is "[t]he level of protection from radiation is expressed in terms of shielding" (*FM 8-10-7* B-1) and is given by the following expression.

$$\frac{I}{I_o} \tag{6.1}$$

This proportion may be regarded as the fraction of dose that penetrates a shield compared to the unshielded dose which varies by shield material and incident photon energy. Protection factors associated with this experiment are compared to the published DoD initial gamma protection factor below.

Table 6.13. Protection Factors for ^{60}Co (*FM 8-10-7* B-2)

Position	ℓ (cm)	Protection Factors			Published Protection Factor
		Experimental	Analytical	Computational	
C1	151.67	0.25	0.45	0.15	0.2
D1	175.70	0.28	0.35	0.11	
B1	255.82	0.02	0.16	0.04	
E1	298.40	INSF	0.16	0.02	
A2	374.11	0.05	0.45	0.06	
C4	385.26	0.03	0.45	0.17	
D4	395.34	0.03	0.43	0.16	
F2	423.43	0.06	0.45	0.17	
A3	425.96	0.16	0.41	0.13	
B4	436.88	0.05	0.40	0.13	
E4	463.11	INSF	0.37	0.12	
F3	469.87	INSF	0.42	0.14	

Table 6.14. Protection Factors for ^{137}Cs (*FM 8-10-7* B-2)

Position	ℓ (cm)	Protection Factors			Published Protection Factor
		Experimental	Analytical	Computational	
C1	151.67	0.17	0.28	0.07	0.2
D1	175.70	0.05	0.19	0.05	
B1	255.82	0.03	0.12	0.01	
E1	298.40	0.05	0.05	0.01	
A2	374.11	INSF	0.28	0.09	
C4	385.26	0.01	0.28	0.09	
D4	395.34	0.03	0.26	0.08	
F2	423.43	0.71	0.28	0.09	
A3	425.96	INSF	0.24	0.06	
B4	436.88	2.13×10^{-3}	0.28	0.06	
E4	463.11	0.03	0.20	0.05	
F3	469.87	0.91	0.25	0.07	

Table 6.15. Protection Factors for ^{226}Ra (*FM 8-10-7* B-2)

Position	ℓ (cm)	Protection Factors			Published Protection Factor
		Experimental	Analytical	Computational	
C1	151.67	0.30	0.09	6.50×10^{-3}	0.2
D1	175.70	0.29	0.04	2.87×10^{-3}	
B1	255.82	0.06	0.02	1.91×10^{-4}	
E1	298.40	0.04	3.47×10^{-3}	3.47×10^{-13}	
A2	374.11	0.01	0.09	3.47×10^{-13}	
C4	385.26	0.03	0.09	8.77×10^{-3}	
D4	395.34	0.07	0.07	7.75×10^{-3}	
F2	423.43	0.01	0.09	9.05×10^{-3}	
A3	425.96	0.19	0.06	7.19×10^{-12}	
B4	436.88	4.34×10^{-3}	0.06	4.65×10^{-3}	
E4	463.11	0.01	0.05	3.37×10^{-3}	
F3	469.87	0.25	0.07	5.41×10^{-3}	

Given that ^{137}Cs is a commonly used source for calibrating and testing DoD radiological equipment, one might reasonably assume that the protection factors provided in *Field Manual No. 8-10-7 Health Service Support in a Nuclear, Biological, and*

Chemical Environment are based on ^{137}Cs (*Test Operations Procedures*). Considering position C1's orientation and proximity to the detector, it is logical to examine the protection factor associated with this point and ^{137}Cs as a comparison. As such, one finds that the experimental protection factor at this point agrees reasonably well with the published value: the experimental value gives a factor of 0.17, a difference of 0.03 from the published DoD initial gamma protection factor, while the analytical and computational values have significantly larger differences from the published value at 0.28 and 0.07 respectively.

6.5 Improvements to the Model

While a considerable number of improvements should be made to the experiment itself in order to yield more reliable results, computational modeling has the potential to be powerful tool in doing so. However, the computational model used here is itself quite rudimentary and also must be improved to be of the greatest value.

The most obvious improvement is the model's geometry. A geometrically complex object such as the M2/M3 BFV has been represented here as a series of rectangular prisms. A more detailed representation would more accurately account for gamma photons that have reached the detector whether by penetration or scattering and account for gamma photons that might have otherwise been absorbed. Consider that the front of the M2/M3 BFV model used here is heavily armored, though in actuality, the front of the vehicle is less likely to be as armored—heavy armor on the front of the vehicle would, of course, complicate maintenance operations and limit access to areas critical to the M2/M3 BFV maintainer. Therefore, one might postulate that more gamma

photons are likely to reach the detector through the front of the vehicle than what this model suggests.

Beyond improving the overall shape of the vehicle, the model could be more detailed with the vehicle's interior. The M2/M3 BFV's interior has been modeled as air. In actuality, the interior of the M2/M3 BFV is quite complex with limited room for crew members. The average density of the vehicle's interior is unquestionably greater than that of air and contributes significantly to photon scatter.

The true identity of the M2/M3 BFV's materials is not known, though this model is based on seemingly reasonable assumptions. However, having access to the exact materials used would certainly further improve accuracy.

The tallies used for this model included the F4 and the F5 tallies, though data analysis only considered the outputs associated with the F4 tallies due to larger than desirable variances associated with the F5 tally outputs. It may well be worth further investigating variance reduction techniques for using the F5 tally in hopes of garnering still more accurate data.

6.6 Detector Response in the Simulated Radiation Field

In reviewing the data associated with the simulated radiation field, no experimental or analytical data is available for comparison, as measurements with the source located at the Z0 position and the AN/VDR-2 located outside of the M2/M3 BFV in an identical position were not taken. Nevertheless, it is worth noting that again, ^{60}Co retains the smallest dose attenuation coefficient, and ^{226}Ra retains the highest.

Table 6.16. Dose Attenuation Coefficients for ^{60}Co Simulated Radiation Field

	ℓ (cm)	I (μGy/h)	I_0 (μGy/h)	μ	Average μ
ICRP 21 1974	106.80	9.94×10^{-19}	9.25×10^{-18}	0.02088	0.02061
ANSI/ANS 6.1.1 1977	106.80	1.40×10^{-18}	1.23×10^{-17}	0.02040	
ICRP 74 1996	106.80	1.19×10^{-18}	1.07×10^{-17}	0.02054	

Table 6.17. Dose Attenuation Coefficients for ^{137}Cs Simulated Radiation Field

	ℓ (cm)	I (μGy/h)	I_0 (μGy/h)	μ	Average μ
ICRP 21 1974	106.80	1.08×10^{-18}	1.56×10^{-17}	0.02500	0.02468
ANSI/ANS 6.1.1 1977	106.80	1.61×10^{-18}	2.18×10^{-17}	0.02440	
ICRP 74 1996	106.80	1.34×10^{-18}	1.86×10^{-17}	0.02463	

Table 6.18. Dose Attenuation Coefficients for ^{226}Ra Simulated Radiation Field

	ℓ (cm)	I (μGy/h)	I_0 (μGy/h)	μ	Average μ
ICRP 21 1974	106.80	4.10×10^{-20}	3.05×10^{-17}	0.06192	0.06174
ANSI/ANS 6.1.1 1977	106.80	7.40×10^{-20}	5.31×10^{-17}	0.06158	
ICRP 74 1996	106.80	5.82×10^{-20}	4.25×10^{-17}	0.06173	

A notable improvement to this model would be altering the source such that the broad disk source does not emit gamma photons in a single, skyward direction. As is, the source does not allow for the photons to scatter as one normally expects with groundshine. However, the monodirectional source was used in this case to ensure that photons passed through the detector cell in a manner consistent with the conditions under which one normally calculates the dose attenuation coefficient.

CHAPTER 7. CONCLUSION

The overall goal of this experiment was to characterize the M2/M3 BFV's attenuation of three gamma photon sources—^{60}Co which generates gamma photons of average energy 1.253 MeV, ^{137}Cs which generates gamma photons of average energy 0.662 MeV, and ^{226}Ra which generates gamma photons of average energy 0.190 MeV. However, due to a considerable number of unknowns about the vehicle's construct, the experiment's exceptionally rudimentary design, use of a less than ideal detector, use of inadequate sources, and several procedural missteps, this experiment's value was limited to its ability to be used as a foundation improve future experiment design and procedure. When compared to data from a basic computational model of the experiment, dose attenuation coefficients calculated experimentally and analytically did not agree well with dose attenuation coefficients based on computational data. Unfortunately, while this experiment gives some ideas as to how much the M2/M3 BFV attenuates gamma photons, it does not definitively answer the question at hand, and future work will be required to generate better, more reliable answers. However, in examining the experimental protection factor associated with position C1 and ^{137}Cs, one finds that the this factor agrees considerably well with published values and lends some insight as to what the true attenuation of the vehicle may be realizing that the beam was not precisely normal to the detector.

Future work must employ appropriate equipment to include a narrow beam collimator, a NaI(Tl) scintillator (or comparable gamma detector), and sources of an appropriate activity. Care must be taken to ensure that the vehicle is in its ideal

configuration for determining attenuation characteristics. That is, all hatches and the rear ramp should be secured as best as possible to ensure that only photons which have penetrated the vehicles walls are allowed to pass to the detector. Also, sources should be placed well away from the detector while determining the background radiation to ensure that source effects are not influencing background measurements. Measurements should be taken with the sources placed at varied distances from the detector rather than the wall of the vehicle, and the detector face must be properly oriented to the beam. That is, the face should be normal to the beam to ensure surface area uniformity. As with any experiment, measurements should be taken and recorded no less than three times to ensure accuracy and allow for validation via statistical analysis. Last but not least, computational modeling is powerful tool that should be used during experiment design to ensure that the experiment is viable and will, in fact, generate data that provides answers to the questions being asked.

APPENDIX A. MCNP INPUT FOR THE COBALT-60 SOURCE AT POSITION A2 WITH THE AN/VDR-2 INTERNALLY INSTALLED

```
M2/M3 Bradley Fighting Vehicle, Co-60, 10 mCi, position A2
c Cell Cards
c ---------------------------------------------------------------------------
c Turret
1  1 -0.001177 (1   -2  3  -4  5 -6) $ Air
2  2 -2.65     (7   -8  9 -10 11 -12) ( -1: 2: -3: 4: -5: 6) $ Aluminum
3  1 -0.001177 (13 -14 15 -16 17 -18) ( -7: 8: -9:10:-11:12) $ Air
4  3 -8.05     (19 -20 21 -22 23 -24) (-13:14:-15:16:-17:18) $ Steel
5  1 -0.001177 (25 -26 27 -28 29 -30) (-19:20:-21:22:-23:24) $ Air
6  3 -8.05     (31 -32 33 -34 35 -36) (-25:26:-27:28:-29:30) $ Steel
c Hull
7  1 -0.001177 (37 -38 39 -40 41 -42) (-79:80:-81:82:-83:84) (85:-86:87) & $ Air
   VOL 19803398.5292
8  2 -2.65     (43 -44 45 -46 47 -48) (-37:38:-39:40:-41:42) $ Aluminum
9  1 -0.001177 (49 -50 51 -52 53 -54) (-43:44:-45:46:-47:48) $ Air
10 3 -8.05     (55 -56 57 -58 59 -60) (-49:50:-51:52:-53:54) $ Steel
11 1 -0.001177 (61 -62 63 -64 65 -66) (-55:56:-57:58:-59:60) $ Air
12 3 -8.05     (67 -68 69 -70 71 -72) (-61:62:-63:64:-65:66) $ Steel
c Armor
13 3 -8.05     (73 -74 75 -76 77 -78) $ Steel
c Engine
14 4 -7.34     (79 -80 81 -82  83 -84) $ Cast Iron
c Detector
15 1 -0.001177 (-85 86 -87) $ Air
c Rear, Universe
16 1 -0.001177 (88   -89  90  -91  92  -93) $ Air
c Front, Universe
17 1 -0.001177 (94   -95  96  -97  98  -99) $ Air
c Left, Universe
18 1 -0.001177 (100 -101 102 -103 104 -105) $ Air
c Right, Universe
19 1 -0.001177 (106 -107 108 -109 110 -111) $ Air
c Underbelly, Universe
20 1 -0.001177 (112 -113 114 -115 116 -117) $ Air
c Universe
21 1 -0.001177 (118 -119 120 -121 122 -123) (32: 89: 95: 101: 107: -73: -112: &
    70:  76:  97: -69:  -90: -114: 72: 78: 93: 99: 111: 117: &
   -71: -77: -92: -98: -104: -116) $ Air
c Graveyard
22 0           (-118: 119: -120: 121: -122: 123) $ Void

c Surface Cards
c ---------------------------------------------------------------------------
c Turret
```

```
1   PZ 171.1 $ Floor
2   PZ 221.9 $ Ceiling
3   PX 111.1 $ Rear
4   PX 304.9 $ Front
5   PY 45.1  $ Left
6   PY 274.9 $ Right
7   PZ 168.6 $ Floor
8   PZ 224.4 $ Ceiling
9   PX 108.6 $ Rear
10  PX 307.4 $ Front
11  PY 42.6  $ Left
12  PY 277.4 $ Right
13  PZ 159.7 $ Floor
14  PZ 233.3 $ Ceiling
15  PX 99.7  $ Rear
16  PX 316.3 $ Front
17  PY 33.7  $ Left
18  PY 286.3 $ Right
19  PZ 159.1 $ Floor
20  PZ 233.9 $ Ceiling
21  PX 99.1  $ Rear
22  PX 316.9 $ Front
23  PY 33.1  $ Left
24  PY 286.9 $ Right
25  PZ 156.6 $ Floor
26  PZ 236.4 $ Ceiling
27  PX 96.6  $ Rear
28  PX 319.4 $ Front
29  PY 30.6  $ Left
30  PY 289.4 $ Right
31  PZ 156   $ Floor
32  PZ 237   $ Ceiling
33  PX 96    $ Rear
34  PX 320   $ Front
35  PY 30    $ Left
36  PY 290   $ Right
c Hull
37  PZ 16.1  $ Floor
38  PZ 140.9 $ Ceiling
39  PX 15.1  $ Rear
40  PX 577.9 $ Front
41  PY 15.1  $ Left
42  PY 304.9 $ Right
43  PZ 13.6  $ Floor
44  PZ 143.4 $ Ceiling
45  PX 12.6  $ Rear
46  PX 580.4 $ Front
47  PY 12.6  $ Left
48  PY 307.4 $ Right
```

```
49  PZ 4.7   $ Floor
50  PZ 152.3 $ Ceiling
51  PX 3.7   $ Rear
52  PX 589.3 $ Front
53  PY 3.7   $ Left
54  PY 316.3 $ Right
55  PZ 4.1   $ Floor
56  PZ 152.9 $ Ceiling
57  PX 3.1   $ Rear
58  PX 589.9 $ Front
59  PY 3.1   $ Left
60  PY 316.9 $ Right
61  PZ 1.6   $ Floor
62  PZ 155.4 $ Ceiling
63  PX 0.6   $ Rear
64  PX 592.4 $ Front
65  PY 0.6   $ Left
66  PY 319.4 $ Right
67  PZ 1     $ Floor
68  PZ 156   $ Ceiling
69  PX 0     $ Rear
70  PX 593   $ Front
71  PY 0     $ Left
72  PY 320   $ Right
c Armor
73  PZ 0     $ Floor
74  PZ 1     $ Ceiling
75  PX 353   $ Rear
76  PX 593   $ Front
77  PY 0     $ Left
78  PY 320   $ Right
c Engine
79  PZ 16.1  $ Floor
80  PZ 55.1  $ Ceiling
81  PX 469   $ Rear
82  PX 570   $ Front
83  PY 135   $ Left
84  PY 275   $ Right
c Detector
85  C/Y 321.3 106.8 1.53
86  PY 39.4  $ Left
87  PY 39.6  $ Right
c Rear, Universe
88  PZ 156   $ Floor
89  PZ 237   $ Ceiling
90  PX 0     $ Rear
91  PX 96    $ Front
92  PY 0     $ Left
93  PY 320   $ Right
```

```
c Front, Universe
94  PZ 156   $ Floor
95  PZ 237   $ Ceiling
96  PX 320   $ Rear
97  PX 593   $ Front
98  PY 0     $ Left
99  PY 320   $ Right
c Left, Universe
100 PZ 156   $ Floor
101 PZ 237   $ Ceiling
102  PX 96    $ Rear
103 PX 320   $ Front
104 PY 0     $ Left
105 PY 30    $ Right
c Right, Universe
106 PZ 156   $ Floor
107 PZ 237   $ Ceiling
108 PX 96    $ Rear
109 PX 320   $ Front
110 PY 290   $ Left
111 PY 320   $ Right
c Underbelly, Universe
112 PZ 0     $ Floor
113 PZ 1     $ Ceiling
114 PX 0     $ Rear
115 PX 353   $ Front
116 PY 0     $ Left
117 PY 320   $ Right
c Boundary, Universe
118 PZ -1000 $ Floor
119 PZ  1237 $ Ceiling
120 PX -1000 $ Rear
121 PX  1593 $ Front
122 PY -1000 $ Left
123 PY  1320 $ Right

c Data Cards
c ---------------------------------------------------------------------------
MODE P
IMP:P 1 1 1 1 1 1 1 1 1 1 1 1 1 1 1 1 1 1 1 1 1 0
SDEF TME=0 PAR=P ERG=d1 WGT=1 CEL=21 POS=693 74 82.3 &
    ARA=3.75 DIR=1 VEC=-371.1 -34.6 24.5
    SI1 L  1.173 1.333
    SP1    0.5   0.5
F054:P  15 $ Average flux in cell 15
F154:P  15 $ Average flux in cell 15
DF154   IC 10 IU 1 FAC 1 LOG $ Fluence-to-dose conversion
F254:P  15 $ Average flux in cell 15
DF254   IC 20 IU 1 FAC 1 LOG $ Fluence-to-dose conversion
```

```
F354:P 15 $ Average flux in cell 15
DE354 0.01  0.015  0.02   0.03   0.04   0.05   0.06   0.08   0.1 & $ ICRP 74 DCC
    0.15   0.2    0.3    0.4    0.5    0.6    0.8    1.     1.5 &
    2.     3.     4.     5.     6.     8.1    10.0
DF354 0.061   0.83   1.05   0.81   0.64   0.55   0.51   0.53     0.61 &
    0.89    1.2    1.8    2.38   2.93   3.44   4.38    5.2   6.9 &
    8.6     11.1   13.4   15.5   17.6   21.6   25.6
F075:P  321.3 39.4 106.8 0.2 $ Point detector in cell 7
F175:P  321.3 39.4 106.8 0.2 $ Point detector in cell 7
DF175   IC 10 IU 1 FAC 1 LOG $ Fluence-to-dose conversion
F275:P  321.3 39.4 106.8 0.2 $ Point detector in cell 7
DF275   IC 20 IU 1 FAC 1 LOG $ Fluence-to-dose conversion
F375:P 321.3 39.4 106.8 0.2 $ Point detector in cell 7
DE375 0.01  0.015  0.02   0.03   0.04   0.05   0.06   0.08   0.1 & $ ICRP 74 DCC
    0.15   0.2    0.3    0.4    0.5    0.6    0.8    1.   1.5 &
    2.     3.     4.     5.     6.     8.1    10.0
DF375 0.061   0.83   1.05   0.81   0.64   0.55   0.51   0.53  0.61 &
    0.89    1.2    1.8    2.38   2.93   3.44   4.38    5.2   6.9 &
    8.6     11.1   13.4   15.5   17.6   21.6   25.6
M1  7000 -0.7808 &  $ Air, nitrogen
    8000 -0.2098 &  $ Air, oxygen
   18000 -0.0093 &  $ Air, argon
    6000 -0.0001    $ Air, carbon
M2 13000 -0.9340 &  $ Aluminum 5083, aluminum
   12000 -0.0445 &  $ Aluminum 5083, magnesium
   25000 -0.007  &  $ Aluminum 5083, manganese
   14000 -0.004  &  $ Aluminum 5083, silicon
   26000 -0.004  &  $ Aluminum 5083, iron
   30000 -0.0025 &  $ Alumimum 5083, zinc
   22000 -0.0015 &  $ Aluminum 5083, titanium
   24000 -0.0015 &  $ Aluminum 5083, chromium
   29000 -0.001     $ Aluminum 5083, copper
M3 26000 -0.99027 & $ UHA Steel, iron
    6000 -0.0032  & $ UHA Steel, carbon
   29000 -0.0025  & $ UHA Steel, copper
   13000 -0.001   & $ UHA Steel, aluminium
   22000 -0.001   & $ UHA Steel, titanium
   40000 -0.001   & $ UHA Steel, zirconium
   15000 -0.0002  & $ UHA Steel, phosphorus
   33000 -0.0002  & $ UHA Steel, arsenic
   50000 -0.0002  & $ UHA Steel, tin
   51000 -0.0002  & $ UHA Steel, antimony
   16000 -0.0001  & $ UHA Steel, sulfur
   82000 -0.0001  & $ UHA Steel, lead
    5000 -0.00003   $ UHA Steel, boron
M4 26000 -0.93415 & $ Cast Iron, iron
    6000 -0.0325  & $ Cast Iron, carbon
   14000 -0.02    & $ Cast Iron, silicon
   15000 -0.006   & $ Cast Iron, phosphorus
```

```
   25000 -0.006   & $ Cast Iron, manganese
   16000 -0.00135   $ Cast Iron, sulfur
NPS 66600000
```

APPENDIX B. MCNP SOURCE DEFINITIONS FOR SOURCES POSITIONED AROUND THE M2/M3 BFV

Cobalt-60

```
A2      SDEF TME=0 PAR=P ERG=d1 WGT=1 CEL=21 POS=693 74 82.3 &
            ARA=3.75 DIR=1 VEC=-371.1 -34.6 24.5
            SI1 L  1.173 1.333
            SP1    0.5   0.5
A3      SDEF TME=0 PAR=P ERG=d1 WGT=1 CEL=21 POS=693 246 82.3 &
            ARA=3.75 DIR=1 VEC=-371.1 -206.6 24.5
            SI1 L  1.173 1.333
            SP1    0.5   0.5
B1      SDEF TME=0 PAR=P ERG=d1 WGT=1 CEL=21 POS=534.4 -100 82.3 &
            ARA=3.75 DIR=1 VEC=-213.1 139.4 24.5
            SI1 L  1.173 1.333
            SP1    0.5   0.5
B4      SDEF TME=0 PAR=P ERG=d1 WGT=1 CEL=21 POS=534.4 420 82.3 &
            ARA=3.75 DIR=1 VEC=-213.1 -380.6 24.5
            SI1 L  1.173 1.333
            SP1    0.5   0.5
C1      SDEF TME=0 PAR=P ERG=d1 WGT=1 CEL=21 POS=375.8 -100 82.3 &
            ARA=3.75 DIR=1 VEC=-54.5 139.4 24.5
            SI1 L  1.173 1.333
            SP1    0.5   0.5
C4      SDEF TME=0 PAR=P ERG=d1 WGT=1 CEL=21 POS=375.8 420 82.3 &
            ARA=3.75 DIR=1 VEC=-54.5 -380.6 24.5
            SI1 L  1.173 1.333
            SP1    0.5   0.5
D1      SDEF TME=0 PAR=P ERG=d1 WGT=1 CEL=21 POS=217.2 -100 82.3 &
            ARA=3.75 DIR=1 VEC=104.1 139.4 24.5
            SI1 L  1.173 1.333
            SP1    0.5   0.5
D4      SDEF TME=0 PAR=P ERG=d1 WGT=1 CEL=21 POS=217.2 420 82.3 &
            ARA=3.75 DIR=1 VEC=104.1 -380.6 24.5
            SI1 L  1.173 1.333
            SP1    0.5   0.5
E1      SDEF TME=0 PAR=P ERG=d1 WGT=1 CEL=21 POS=58.6 -100 82.3 &
            ARA=3.75 DIR=1 VEC=262.7 139.4 24.5
            SI1 L  1.173 1.333
            SP1    0.5   0.5
E4      SDEF TME=0 PAR=P ERG=d1 WGT=1 CEL=21 POS=58.6 420 82.3 &
            ARA=3.75 DIR=1 VEC=262.7 -380.6 24.5
            SI1 L  1.173 1.333
            SP1    0.5   0.5
F2      SDEF TME=0 PAR=P ERG=d1 WGT=1 CEL=21 POS=-100 74 82.3 &
            ARA=3.75 DIR=1 VEC=421.3 -34.6 24.5
            SI1 L  1.173 1.333
            SP1    0.5   0.5
F3      SDEF TME=0 PAR=P ERG=d1 WGT=1 CEL=21 POS=-100 246 82.3 &
            ARA=3.75 DIR=1 VEC=421.3 -206.6 24.5
            SI1 L  1.173 1.333
            SP1    0.5   0.5
```

Cesium-137

```
A2      SDEF TME=0 PAR=P ERG=d1 WGT=1 CEL=21 POS=693 74 82.3 &
            ARA=3.75 DIR=1 VEC=-371.7 -34.6 24.5
            SI1 L  0.662
            SP1    1
A3      SDEF TME=0 PAR=P ERG=d1 WGT=1 CEL=21 POS=693 246 82.3 &
            ARA=3.75 DIR=1 VEC=-371.7 -206.6 24.5
            SI1 L  0.662
            SP1    1
B1      SDEF TME=0 PAR=P ERG=d1 WGT=1 CEL=21 POS=534.4 -100 82.3 &
            ARA=3.75 DIR=1 VEC=-213.1 139.4 24.5
            SI1 L  0.662
            SP1    1
B4      SDEF TME=0 PAR=P ERG=d1 WGT=1 CEL=21 POS=534.4 420 82.3 &
            ARA=3.75 DIR=1 VEC=-213.1 -380.6 24.5
            SI1 L  0.662
            SP1    1
C1      SDEF TME=0 PAR=P ERG=d1 WGT=1 CEL=21 POS=375.8 -100 82.3 &
            ARA=3.75 DIR=1 VEC=-54.5 139.4 24.5
            SI1 L  0.662
            SP1    1
C4      SDEF TME=0 PAR=P ERG=d1 WGT=1 CEL=21 POS=375.8 420 82.3 &
            ARA=3.75 DIR=1 VEC=-54.5 -380.6 24.5
            SI1 L  0.662
            SP1    1
D1      SDEF TME=0 PAR=P ERG=d1 WGT=1 CEL=21 POS=217.2 -100 82.3 &
            ARA=3.75 DIR=1 VEC=104.1 139.4 24.5
            SI1 L  0.662
            SP1    1
D4      SDEF TME=0 PAR=P ERG=d1 WGT=1 CEL=21 POS=217.2 420 82.3 &
            ARA=3.75 DIR=1 VEC=104.1 -380.6 24.5
            SI1 L  0.662
            SP1    1
E1      SDEF TME=0 PAR=P ERG=d1 WGT=1 CEL=21 POS=58.6 -100 82.3 &
            ARA=3.75 DIR=1 VEC=262.7 139.4 24.5
            SI1 L  0.662
            SP1    1
E4      SDEF TME=0 PAR=P ERG=d1 WGT=1 CEL=21 POS=58.6 420 82.3 &
            ARA=3.75 DIR=1 VEC=262.7 -380.6 24.5
            SI1 L  0.662
            SP1    1
F2      SDEF TME=0 PAR=P ERG=d1 WGT=1 CEL=21 POS=-100 74 82.3 &
            ARA=3.75 DIR=1 VEC=421.3 -34.6 24.5
            SI1 L  0.662
            SP1    1
F3      SDEF TME=0 PAR=P ERG=d1 WGT=1 CEL=21 POS=-100 246 82.3 &
            ARA=3.75 DIR=1 VEC=421.3 -206.6 24.5
            SI1 L  0.662
            SP1    1
```

Radium-226

```
A2      SDEF TME=0 PAR=P ERG=d1 WGT=1 CEL=21 POS=693 74 82.3 &
            ARA=3.75 DIR=1 VEC-371.7 -34.6 24.5
            SI1 L  0.18610 0.26227 0.60066
            SP1    0.99847 0.00139 0.00014
A3      SDEF TME=0 PAR=P ERG=d1 WGT=1 CEL=21 POS=693 246 82.3 &
            ARA=3.75 DIR=1 VEC-371.7 -206.6 24.5
            SI1 L  0.18610 0.26227 0.60066
            SP1    0.99847 0.00139 0.00014
B1      SDEF TME=0 PAR=P ERG=d1 WGT=1 CEL=21 POS=534.4 -100 82.3 &
            ARA=3.75 DIR=1 VEC=-213.1 139.4 24.5
            SI1 L  0.18610 0.26227 0.60066
            SP1    0.99847 0.00139 0.00014
B4      SDEF TME=0 PAR=P ERG=d1 WGT=1 CEL=21 POS=534.4 420 82.3 &
            ARA=3.75 DIR=1 VEC=-213.1 -380.6 24.5
            SI1 L  0.18610 0.26227 0.60066
            SP1    0.99847 0.00139 0.00014
C1      SDEF TME=0 PAR=P ERG=d1 WGT=1 CEL=21 POS=375.8 -100 82.3 &
            ARA=3.75 DIR=1 VEC=-54.5 139.4 24.5
            SI1 L  0.18610 0.26227 0.60066
            SP1    0.99847 0.00139 0.00014
C4      SDEF TME=0 PAR=P ERG=d1 WGT=1 CEL=21 POS=375.8 420 82.3 &
            ARA=3.75 DIR=1 VEC=-54.5 -380.6 24.5
            SI1 L  0.18610 0.26227 0.60066
            SP1    0.99847 0.00139 0.00014
D1      SDEF TME=0 PAR=P ERG=d1 WGT=1 CEL=21 POS=217.2 -100 82.3 &
            ARA=3.75 DIR=1 VEC=104.1 139.4 24.5
            SI1 L  0.18610 0.26227 0.60066
            SP1    0.99847 0.00139 0.00014
D4      SDEF TME=0 PAR=P ERG=d1 WGT=1 CEL=21 POS=217.2 420 82.3 &
            ARA=3.75 DIR=1 VEC=104.1 -380.6 24.5
            SI1 L  0.18610 0.26227 0.60066
            SP1    0.99847 0.00139 0.00014
E1      SDEF TME=0 PAR=P ERG=d1 WGT=1 CEL=21 POS=58.6 -100 82.3 &
            ARA=3.75 DIR=1 VEC=262.7 139.4 24.5
            SI1 L  0.18610 0.26227 0.60066
            SP1    0.99847 0.00139 0.00014
E4      SDEF TME=0 PAR=P ERG=d1 WGT=1 CEL=21 POS=58.6 420 82.3 &
            ARA=3.75 DIR=1 VEC=262.7 -380.6 24.5
            SI1 L  0.18610 0.26227 0.60066
            SP1    0.99847 0.00139 0.00014
F2      SDEF TME=0 PAR=P ERG=d1 WGT=1 CEL=21 POS=-100 74 82.3 &
            ARA=3.75 DIR=1 VEC 421.3 -34.6 24.5
            SI1 L  0.18610 0.26227 0.60066
            SP1    0.99847 0.00139 0.00014
F3      SDEF TME=0 PAR=P ERG=d1 WGT=1 CEL=21 POS=-100 246 82.3 &
            ARA=3.75 DIR=1 VEC 421.3 -206.6 24.5
            SI1 L  0.18610 0.26227 0.60066
            SP1    0.99847 0.00139 0.00014
```

APPENDIX C. MCNP INPUT FOR THE COBALT-60 SIMULATED RADIATION FIELD WITH THE AN/VDR-2 INTERNALLY INSTALLED

```
M2/M3 Bradley Fighting Vehicle, Co-60, 10 mCi, Radiation Field
c Cell Cards
c ---------------------------------------------------------------------------
c Turret
1  1 -0.001177 (1   -2  3  -4  5 -6) $ Air
2  2 -2.65     (7   -8  9 -10 11 -12) ( -1: 2: -3: 4: -5: 6) $ Aluminum
3  1 -0.001177 (13 -14 15 -16 17 -18) ( -7: 8: -9:10:-11:12) $ Air
4  3 -8.05     (19 -20 21 -22 23 -24) (-13:14:-15:16:-17:18) $ Steel
5  1 -0.001177 (25 -26 27 -28 29 -30) (-19:20:-21:22:-23:24) $ Air
6  3 -8.05     (31 -32 33 -34 35 -36) (-25:26:-27:28:-29:30) $ Steel
c Hull
7  1 -0.001177 (37 -38 39 -40 41 -42) (-79:80:-81:82:-83:84) (85:-86:87) & $ Air
   VOL 19803398.5292
8  2 -2.65     (43 -44 45 -46 47 -48) (-37:38:-39:40:-41:42) $ Aluminum
9  1 -0.001177 (49 -50 51 -52 53 -54) (-43:44:-45:46:-47:48) $ Air
10 3 -8.05     (55 -56 57 -58 59 -60) (-49:50:-51:52:-53:54) $ Steel
11 1 -0.001177 (61 -62 63 -64 65 -66) (-55:56:-57:58:-59:60) $ Air
12 3 -8.05     (67 -68 69 -70 71 -72) (-61:62:-63:64:-65:66) $ Steel
c Armor
13 3 -8.05     (73 -74 75 -76 77 -78) $ Steel
c Engine
14 4 -7.34     (79 -80 81 -82  83 -84) $ Cast Iron
c Detector
15 1 -0.001177 (-85 86 -87) $ Air
c Rear, Universe
16 1 -0.001177 (88   -89  90  -91  92  -93) $ Air
c Front, Universe
17 1 -0.001177 (94   -95  96  -97  98  -99) $ Air
c Left, Universe
18 1 -0.001177 (100 -101 102 -103 104 -105) $ Air
c Right, Universe
19 1 -0.001177 (106 -107 108 -109 110 -111) $ Air
c Underbelly, Universe
20 1 -0.001177 (112 -113 114 -115 116 -117) $ Air
c Universe
21 1 -0.001177 (118 -119 120 -121 122 -123) (32: 89: 95: 101: 107: -73: -112: &
    70:  76:  97: -69:  -90: -114: 72: 78: 93: 99: 111: 117: &
   -71: -77: -92: -98: -104: -116) $ Air
c Graveyard
22 0           (-118: 119: -120: 121: -122: 123) $ Void

c Surface Cards
c ---------------------------------------------------------------------------
```

```
c Turret
1   PZ 171.1 $ Floor
2   PZ 221.9 $ Ceiling
3   PX 111.1 $ Rear
4   PX 304.9 $ Front
5   PY 45.1  $ Left
6   PY 274.9 $ Right
7   PZ 168.6 $ Floor
8   PZ 224.4 $ Ceiling
9   PX 108.6 $ Rear
10  PX 307.4 $ Front
11  PY 42.6  $ Left
12  PY 277.4 $ Right
13  PZ 159.7 $ Floor
14  PZ 233.3 $ Ceiling
15  PX 99.7  $ Rear
16  PX 316.3 $ Front
17  PY 33.7  $ Left
18  PY 286.3 $ Right
19  PZ 159.1 $ Floor
20  PZ 233.9 $ Ceiling
21  PX 99.1  $ Rear
22  PX 316.9 $ Front
23  PY 33.1  $ Left
24  PY 286.9 $ Right
25  PZ 156.6 $ Floor
26  PZ 236.4 $ Ceiling
27  PX 96.6  $ Rear
28  PX 319.4 $ Front
29  PY 30.6  $ Left
30  PY 289.4 $ Right
31  PZ 156   $ Floor
32  PZ 237   $ Ceiling
33  PX 96    $ Rear
34  PX 320   $ Front
35  PY 30    $ Left
36  PY 290   $ Right
c Hull
37  PZ 16.1  $ Floor
38  PZ 140.9 $ Ceiling
39  PX 15.1  $ Rear
40  PX 577.9 $ Front
41  PY 15.1  $ Left
42  PY 304.9 $ Right
43  PZ 13.6  $ Floor
44  PZ 143.4 $ Ceiling
45  PX 12.6  $ Rear
46  PX 580.4 $ Front
47  PY 12.6  $ Left
```

```
48  PY 307.4 $ Right
49  PZ 4.7   $ Floor
50  PZ 152.3 $ Ceiling
51  PX 3.7   $ Rear
52  PX 589.3 $ Front
53  PY 3.7   $ Left
54  PY 316.3 $ Right
55  PZ 4.1   $ Floor
56  PZ 152.9 $ Ceiling
57  PX 3.1   $ Rear
58  PX 589.9 $ Front
59  PY 3.1   $ Left
60  PY 316.9 $ Right
61  PZ 1.6   $ Floor
62  PZ 155.4 $ Ceiling
63  PX 0.6   $ Rear
64  PX 592.4 $ Front
65  PY 0.6   $ Left
66  PY 319.4 $ Right
67  PZ 1     $ Floor
68  PZ 156   $ Ceiling
69  PX 0     $ Rear
70  PX 593   $ Front
71  PY 0     $ Left
72  PY 320   $ Right
c Armor
73  PZ 0     $ Floor
74  PZ 1     $ Ceiling
75  PX 353   $ Rear
76  PX 593   $ Front
77  PY 0     $ Left
78  PY 320   $ Right
c Engine
79  PZ 16.1  $ Floor
80  PZ 55.1  $ Ceiling
81  PX 469   $ Rear
82  PX 570   $ Front
83  PY 135   $ Left
84  PY 275   $ Right
c Detector
85  C/Y 321.3 106.8 1.53
86  PY 39.4  $ Left
87  PY 39.6  $ Right
c Rear, Universe
88  PZ 156   $ Floor
89  PZ 237   $ Ceiling
90  PX 0     $ Rear
91  PX 96    $ Front
92  PY 0     $ Left
```

```
93  PY 320   $ Right
c Front, Universe
94  PZ 156   $ Floor
95  PZ 237   $ Ceiling
96  PX 320   $ Rear
97  PX 593   $ Front
98  PY 0     $ Left
99  PY 320   $ Right
c Left, Universe
100 PZ 156   $ Floor
101 PZ 237   $ Ceiling
102  PX 96    $ Rear
103 PX 320   $ Front
104 PY 0     $ Left
105 PY 30    $ Right
c Right, Universe
106 PZ 156   $ Floor
107 PZ 237   $ Ceiling
108 PX 96    $ Rear
109 PX 320   $ Front
110 PY 290   $ Left
111 PY 320   $ Right
c Underbelly, Universe
112 PZ 0     $ Floor
113 PZ 1     $ Ceiling
114 PX 0     $ Rear
115 PX 353   $ Front
116 PY 0     $ Left
117 PY 320   $ Right
c Boundary, Universe
118 PZ -1000 $ Floor
119 PZ  1237 $ Ceiling
120 PX -1000 $ Rear
121 PX  1593 $ Front
122 PY -1000 $ Left
123 PY  1320 $ Right

c Data Cards
c ---------------------------------------------------------------------------
MODE P
IMP:P 2 2 2 2 2 2 2 2 2 2 2 2 2 2 3 1 1 1 1 1 1 0
SDEF TME=0 PAR=P ERG=d1 WGT=1 CEL=21 POS=296.5 160 0 &
    ARA=7.8539816339745E+05  DIR=1 VEC=0 0 1  AXS=0 0 1  EXT=0 RAD=d2
    SI1 L  1.173 1.333
    SP1    0.5   0.5
    SI2    0     500
    SP2   -21    1
F054:P  15 $ Average flux in cell 15
F154:P  15 $ Average flux in cell 15
```

```
DF154   IC 10 IU 1 FAC 1 LOG $ Fluence-to-dose conversion
F254:P  15 $ Average flux in cell 15
DF254   IC 20 IU 1 FAC 1 LOG $ Fluence-to-dose conversion
F354:P 15 $ Average flux in cell 15
DE354 0.01  0.015  0.02   0.03   0.04   0.05   0.06   0.08   0.1 & $ ICRP 74 DCC
    0.15   0.2    0.3    0.4    0.5    0.6    0.8    1.     1.5 &
    2.     3.     4.     5.     6.     8.1    10.0
DF354 0.061   0.83   1.05   0.81   0.64   0.55   0.51   0.53     0.61 &
    0.89    1.2    1.8    2.38   2.93   3.44   4.38    5.2   6.9 &
    8.6     11.1   13.4   15.5   17.6   21.6   25.6
F075:P  321.3 39.4 106.8 0.2 $ Point detector in cell 7
F175:P  321.3 39.4 106.8 0.2 $ Point detector in cell 7
DF175   IC 10 IU 1 FAC 1 LOG $ Fluence-to-dose conversion
F275:P  321.3 39.4 106.8 0.2 $ Point detector in cell 7
DF275   IC 20 IU 1 FAC 1 LOG $ Fluence-to-dose conversion
F375:P 321.3 39.4 106.8 0.2 $ Point detector in cell 7
DE375 0.01  0.015  0.02   0.03   0.04   0.05   0.06   0.08   0.1 & $ ICRP 74 DCC
    0.15   0.2    0.3    0.4    0.5    0.6    0.8    1.   1.5 &
    2.     3.     4.     5.     6.     8.1    10.0
DF375 0.061   0.83   1.05   0.81   0.64   0.55   0.51   0.53  0.61 &
    0.89    1.2    1.8    2.38   2.93   3.44   4.38    5.2   6.9 &
    8.6     11.1   13.4   15.5   17.6   21.6   25.6
M1  7000 -0.7808 &  $ Air, nitrogen
    8000 -0.2098 &  $ Air, oxygen
   18000 -0.0093 &  $ Air, argon
    6000 -0.0001    $ Air, carbon
M2 13000 -0.9340 &  $ Aluminum 5083, aluminum
   12000 -0.0445 &  $ Aluminum 5083, magnesium
   25000 -0.007  &  $ Aluminum 5083, manganese
   14000 -0.004  &  $ Aluminum 5083, silicon
   26000 -0.004  &  $ Aluminum 5083, iron
   30000 -0.0025 &  $ Alumimum 5083, zinc
   22000 -0.0015 &  $ Aluminum 5083, titanium
   24000 -0.0015 &  $ Aluminum 5083, chromium
   29000 -0.001     $ Aluminum 5083, copper
M3 26000 -0.99027 & $ UHA Steel, iron
    6000 -0.0032  & $ UHA Steel, carbon
   29000 -0.0025  & $ UHA Steel, copper
   13000 -0.001   & $ UHA Steel, aluminium
   22000 -0.001   & $ UHA Steel, titanium
   40000 -0.001   & $ UHA Steel, zirconium
   15000 -0.0002  & $ UHA Steel, phosphorus
   33000 -0.0002  & $ UHA Steel, arsenic
   50000 -0.0002  & $ UHA Steel, tin
   51000 -0.0002  & $ UHA Steel, antimony
   16000 -0.0001  & $ UHA Steel, sulfur
   82000 -0.0001  & $ UHA Steel, lead
    5000 -0.00003   $ UHA Steel, boron
M4 26000 -0.93415 & $ Cast Iron, iron
```

```
     6000 -0.0325  & $ Cast Iron, carbon
    14000 -0.02    & $ Cast Iron, silicon
    15000 -0.006   & $ Cast Iron, phosphorus
    25000 -0.006   & $ Cast Iron, manganese
    16000 -0.00135   $ Cast Iron, sulfur
NPS 1E+10
```

APPENDIX D. MCNP SOURCE DEFINITIONS FOR THE SIMULATED RADIATION FIELD

Cobalt-60

```
SDEF TME=0 PAR=P ERG=d1 WGT=1 CEL=21 POS=296.5 160 0 &
    ARA=7.8539816339745E+05  DIR=1 VEC=0 0 1  AXS=0 0 1  EXT=0 RAD=d2
    SI1 L  1.173 1.333
    SP1    0.5   0.5
    SI2    0     500
    SP2   -21    1
```

Cesium-137

```
SDEF TME=0 PAR=P ERG=d1 WGT=1 CEL=21 POS=296.5 160 0 &
    ARA=7.8539816339745E+05  DIR=1 VEC=0 0 1  AXS=0 0 1  EXT=0 RAD=d2
    SI1 L  0.662
    SP1    1
    SI2    0     500
    SP2   -21    1
```

Radium-226

```
SDEF TME=0 PAR=P ERG=d1 WGT=1 CEL=21 POS=296.5 160 0 &
    ARA=7.8539816339745E+05  DIR=1 VEC=0 0 1  AXS=0 0 1  EXT=0 RAD=d2
    SI1 L  0.18610 0.26227 0.60066
    SP1    0.99847 0.00139 0.00014
    SI2    0     500
    SP2   -21    1
```

APPENDIX E. A REVISED COMPARISON OF THE EXPERIMENTAL, ANALYTICAL, AND COMPUTATIONAL DOSE ATTENUATION COEFFICIENTS

In an effort to obtain liner attenuation coefficients for positions whose net absorbed dose rate generated negative values, a trimmed average for the background absorbed dose rates has been used here.

(continued on next page)

Table E.1. Revised Dose Attenuation Coefficients for ^{60}Co

Position	ℓ (cm)	μ			Standard Deviation, σ
		Experimental	Analytical	Computational	
C1	151.67	0.00917	0.01615	0.01253	0.00345
D1	175.70	0.00740	0.02521	0.01255	0.00921
B1	255.82	0.01139	0.01652	0.01257	0.00197
E1	298.40	0.00925	0.02951	0.01257	0.01198
A2	374.11	0.00785	0.00288	0.00738	0.00283
C4	385.26	0.00883	0.00277	0.00461	0.00334
D4	395.34	0.01048	0.00292	0.00461	0.00320
F2	423.43	0.00869	0.00245	0.00417	0.00204
A3	425.96	0.00430	0.00289	0.00473	0.00096
B4	436.88	0.00718	0.00287	0.00461	0.00203
E4	463.11	INSF	0.00297	0.00461	0.00116
F3	469.87	INSF	0.00240	0.00417	0.00125

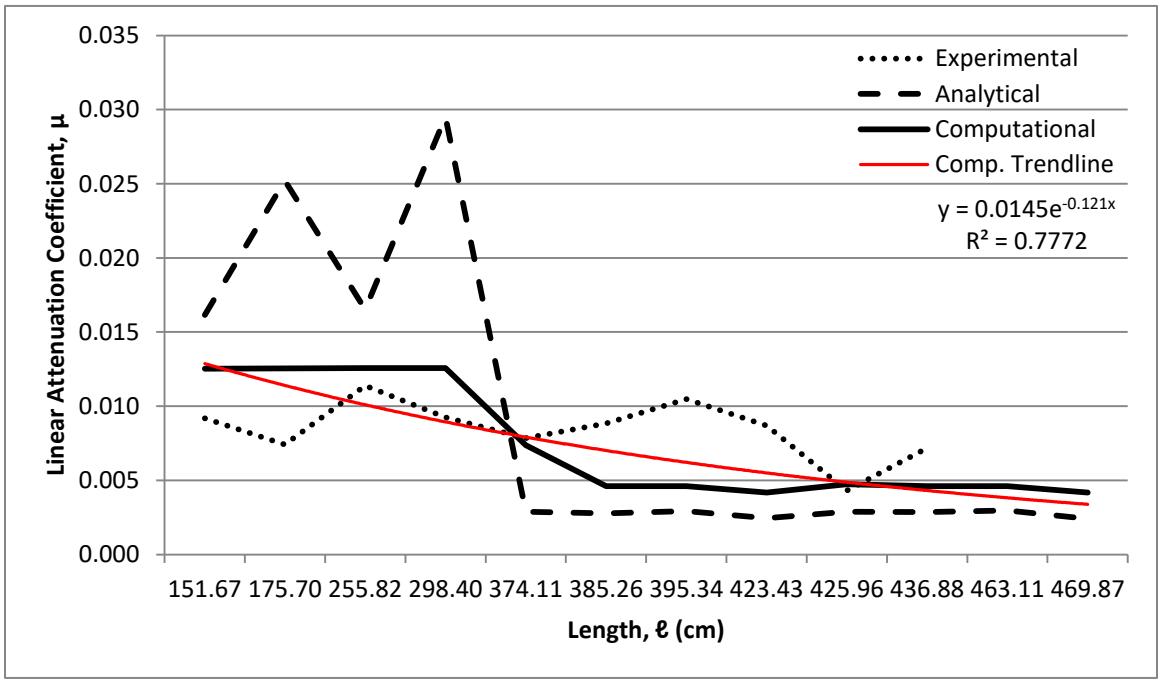

Figure E.1. Revised Plot of Length vs. Dose Attenuation Coefficient for ^{60}Co

Table E.2. Revised Dose Attenuation Coefficients for ^{137}Cs

Position	ℓ (cm)	μ			Standard Deviation, σ
		Experimental	Analytical	Computational	
C1	151.67	0.01186	0.02592	0.01713	0.0072
D1	175.70	0.01766	0.04046	0.01716	0.0134
B1	255.82	0.01448	0.02650	0.01720	0.0065
E1	298.40	0.01107	0.04735	0.01721	0.0197
A2	374.11	0.01675	0.00461	0.00647	0.0013
C4	385.26	0.01177	0.00442	0.00632	0.0045
D4	395.34	0.00851	0.00468	0.00632	0.0019
F2	423.43	0.00052	0.00391	0.00571	0.0025
A3	425.96	0.01877	0.00462	0.00647	0.0013
B4	436.88	0.01462	0.00459	0.00632	0.0051
E4	463.11	0.00890	0.00475	0.00632	0.0015
F3	469.87	0.00027	0.00384	0.00571	0.0028

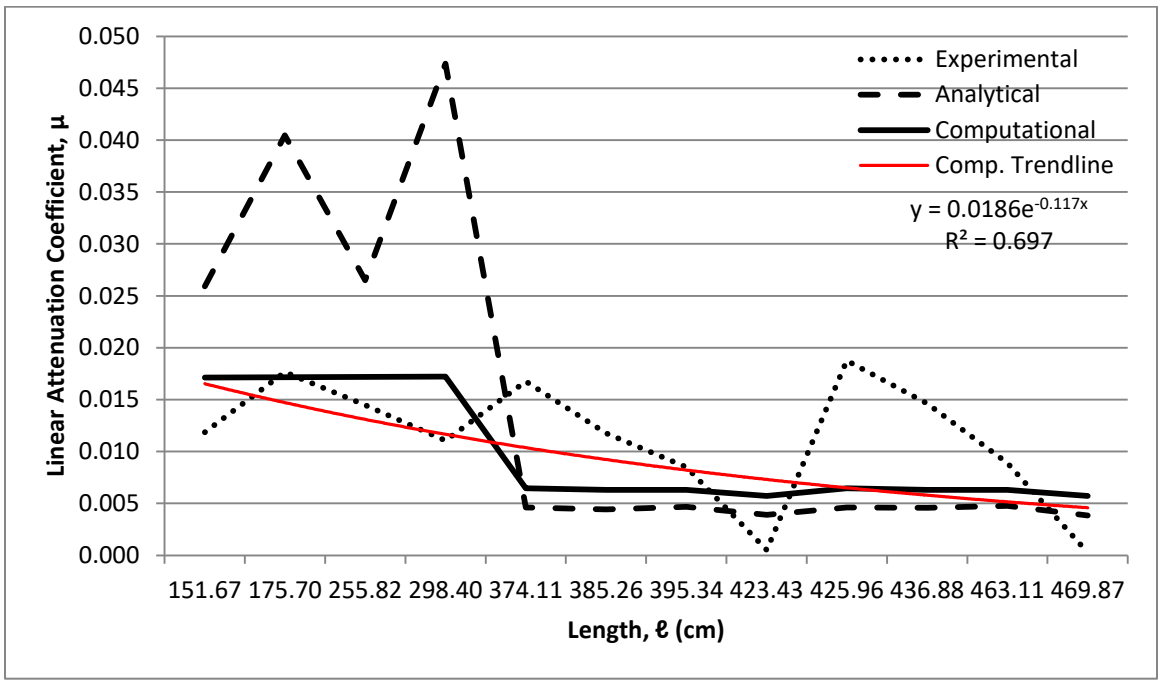

Figure E.2. Revised Plot of Length vs. Dose Attenuation Coefficient for ^{137}Cs

Table E.3. Revised Dose Attenuation Coefficients for ^{226}Ra

Position	ℓ (cm)	μ			Standard Deviation, σ
		Experimental	Analytical	Computational	
C1	151.67	0.00784	0.05017	0.03321	0.0213
D1	175.70	0.00755	0.07833	0.03321	0.0361
B1	255.82	0.01125	0.05129	0.03347	0.0201
E1	298.40	0.00883	0.09168	0.03350	0.0418
A2	374.11	0.00815	0.00890	0.07669	0.0384
C4	385.26	0.00769	0.00854	0.01229	0.0021
D4	395.34	0.00744	0.00903	0.01229	0.0028
F2	423.43	0.01055	0.00755	0.01111	0.0022
A3	425.96	0.00404	0.00892	0.06024	0.0312
B4	436.88	0.00970	0.00885	0.01229	0.0020
E4	463.11	0.01039	0.00917	0.01229	0.0017
F3	469.87	0.01150	0.00741	0.01111	0.0041

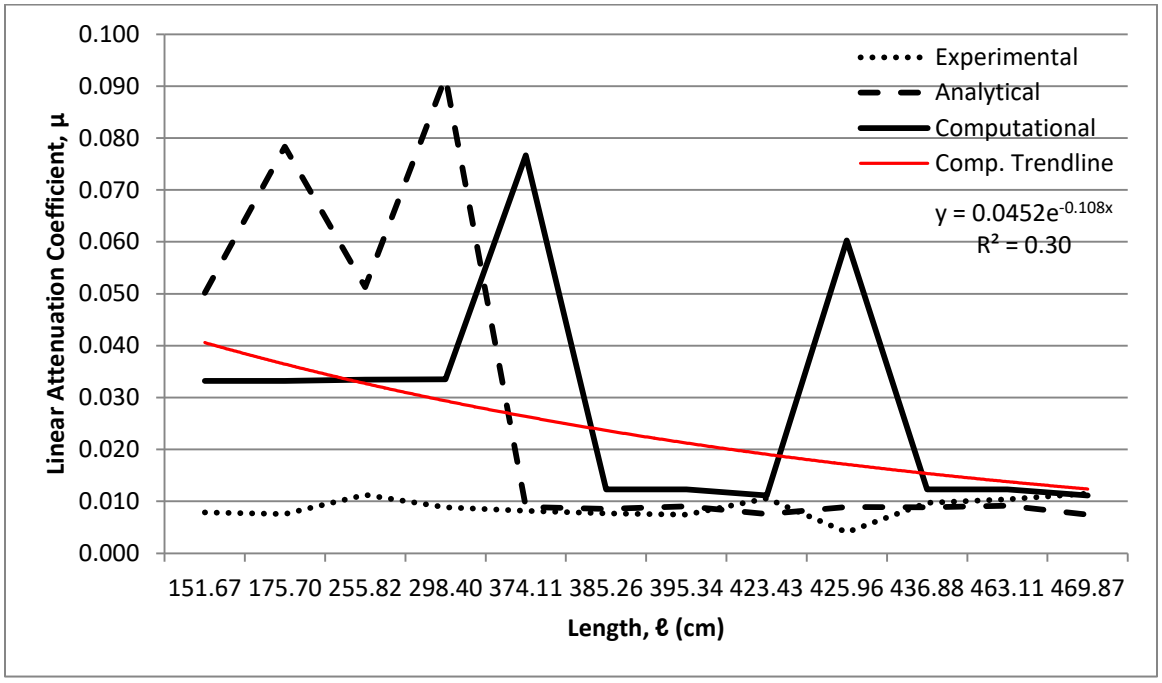

Figure E.3. Revised Plot of Length vs. Dose Attenuation Coefficient for ^{226}Ra

REFERENCES

"^{131}I Iodine." *Live Chart of Nuclides.* International Atomic Energy Agency. Web. 7 Apr. 2018.

"^{137}Cs Cesium." *Live Chart of Nuclides.* International Atomic Energy Agency. Web. 30 May 2017.

"^{226}Ra Radium." *Live Chart of Nuclides.* International Atomic Energy Agency. Web. 30 May 2017.

"^{60}Co Cobalt." *Live Chart of Nuclides.* International Atomic Energy Agency. Web. 30 May 2017.

"Air - Composition and Molecular Weight." *The Engineering ToolBox.* Web. 16 Feb. 2018.

"Air - Density, Specific Weight and Thermal Expansion Coefficient at Varying Temperature and Constant Pressures." *The Engineering ToolBox*. Web. 4 Feb. 2018.

Aluminum Alloys - Aluminum 5083 Properties, Fabrication and Applications, Supplier Data by Aalco. Aalco, 2005.

Athens, Tony. ""Marine Age" the REAL age of a Marine Diesel Engine." *Seaboard Marine*. Web. 31 Jan. 2018.

Buyuk, Bulent. "Gamma Attenuation Behavior of Some Stainless and Boron Steels." *Acta Physica Polonica Series*, 127.4 (2015): 1342-45. Polish Academy of Sciences Institute of Physics. Web. 19 Mar. 2018.

Caner, Zafer and Mustafa Çağatay Tufan. "Investigation of Attenuation Coefficients of Some Stainless Steel and Aluminum Alloys." *AIP Conference Proceedings*, 1935.1 (2018): 180002-1-5. American Institute of Physics. Web. 19 Mar. 2018.

Chabot, George E. "Shielding of Gamma Radiation." *The Health Physics Society*. 22 Aug. 2007. Web. 7 Apr. 2018.

Chilton, Arthur B. et al. *Principles of Radiation Shielding*. Englewood Cliffs: Prentice-Hall, Inc., 1984. Print.

"Co 60 Decay Scheme." *Nucleonica*, Nucleonica Wiki, 25 Feb. 2015. Web. 19 Mar. 2018.

"Computational Modeling." *National Institute of Biomedical Imaging and Bioengineering*. U.S. Department of Health & Human Services, Sep. 2016. Web. 8 Apr. 2018.

Connors, Kevin. "Infantry Fighting Vehicle M2 Bradley." *The American Fighting Vehicle Database*. Web. 3 Apr. 2018.

"Cs 137 Decay Scheme." *Nucleonica*, Nucleonica Wiki, 25 Feb. 2015. Web. 19 Mar. 2018.

Detail Specification Armor Plate, Steel, Wrought High hardness. Defense Standardization Program. 2009.

Eastburg, Amy J. *Assessing the Dose After a Radiological Dispersal Device (RDD) Attack Using a Military RADIAC Instrument*. MS Thesis. Georgia Institute of Technology, 2010. Web. 30 May 2017.

Elert, Glenn, ed. "Density of Steel." *The Physics Factbook: An encyclopedia of scientific essays.* 4 Feb. 2018.

Estimates and Evaluation of Fallout in the United States From Nuclear Weapons Testing Conducted through 1962. Washington, D.C.: Federal Radiation Council, 1963. Web. 7 Apr. 2018.

Field Manual No. 8-10-7 Health Service Support in a Nuclear, Biological, and Chemical Environment. Washington, DC.: United States Army Publishing Directorate, 1993. Print.

Gamma Radiation Dose Rate Conversions. Center for Radiological Nuclear Training at the Nevada National Security Site. Web. 26 Feb. 2018.

Hertel, Nolan E. "MCNP." Message to Desirée R. Prince. 27 Feb. 2018. E-mail.

---. Personal Interview. 3 Apr. 2018.

"How Geiger Counters Work and Detect Nuclear Radiation." *Images Scientific Instruments*. Web. 4 Apr. 2018.

Hunnicut, R. P. *Bradley: A History of American Fighting and Support Vehicles*. Novato: Presidio Press. 1999. Print.

"I 131 Decay Scheme." *Nucleonica,* Nucleonica Wiki, 25 Feb. 2015. Web. 13 Apr. 2018.

Introduction to Cast Iron: History, Types, Properties, and Uses." *Reliance Foundry*. Web. 4 Feb. 2018.

Knoll, Glenn F. *Radiation Detection and Measurement*. John Wiley & Sons, Inc., 2010. Print.

Madbouly, A. M. and E. R. Atta. "Comparative Study between Lead Oxide and Lead Nitrate Polymer as Gamma-Radiation Shielding Materials." *Journal of Environmental Protection* 7.2 (2016): 268-76. Scientific Research. Web. 15 Apr. 2018.

Overview of Materials for Gray Cast Iron." *MatWeb.* 4 Apr. 2018.

"Pair production." *Encyclopædia Brittanica*. Encyclopædia Britannica, Inc., 2008. Web. 20 Apr. 2018.

Pelowitz, Denise B., ed. *MCNP6™ User's Manual Version 1.0.* Los Alamos: Los Alamos National Security, LLC, 2008. PDF document.

Photograph of the DT-616 Probe. *Argon Electronics*. Web. 4 Apr. 2018.

Pike, John. "M2A3 and M3A3 Bradley Fighting Vehicle Systems (BFVS) Specifications." *GlobalSecurity.Org.* Web. 29 Jan. 2018.

Poškus, Andrius. *Attenuation of Gamma Rays*. Vilnius, Lithuania: Vilnius University. Web. 3 Apr. 2018.

"Ra 226 Decay Scheme." *Nucleonica*, Nucleonica Wiki, 25 Feb. 2015. Web. 20 Apr. 2018.

"Radiation Basics." *United States Nuclear Regulatory Commission*. Web. 4 Apr. 2018.

Radiographic Inspection – Formula Based on Newton's Inverse Square Law." *NDT Resource Center*. The Collaboration for NDT Education, Iowa State University. Web. 16 Mar. 18.

Ryan, Shannon, et al. "The ballistic performance of an ultra-high hardness armour steel: An experimental Investigation." *International Journal of Impact Engineering* 94 (2016): 60-73. Elsevier. Web. 4 Feb. 2018.

Shielding Radiation: Alphas, Betas, Gammas and Neutrons." *United States Nuclear Regulatory Commission.* Web. 7 Apr. 2018.

Smart, Jeffery K. *History of Chemical and Biological Detectors, Alarms and Warning Systems*. Aberdeen Proving Ground: United States Army Publishing Directorate. Print.

Standards for Protection Against Radiation." 10 "CFR" 20.1004. 2015.

Stewart, Richard W., ed. *American Military History, Volume II*. Washington, D.C., United States Army Publishing Directorate, 2005.

Technical Manual No. 11-6665-251-10 Operator's Manual RADIAC Set AN/VDR-2. Washington, D.C.: United States Army Publishing Directorate, 1988. Print.

Technical Manual No. 11-6665-251-20 Organizational Maintenance Manual RADIAC Set AN/VDR-2. Washington, D.C.: United States Army Publishing Directorate, 1988. Print.

Technical Manual No. 9-2350-252-10-1 Operator's Manual Fighting Vehicle, Infantry M2 and Fighting Vehicle, Infantry Hull. Washington, DC.: United States Army Publishing Directorate, 1986. Print.

Technical Manual No. 9-2350-252-10-2 Operator's Manual Fighting Vehicle, Infantry M2 and Fighting Vehicle, Infantry Turret. Washington, DC.: United States Army Publishing Directorate, 1985. Print.

*Test and Evaluation Capabilities and Methodologies Integrated Process Team Test Operations Procedures for Radiation Detection Systems – Specific Methods***.** Arlington: Department of Defense, 2012. Web. 25 Apr. 2018.

"Transmitted Intensity and Linear Attenuation Coefficient." *NDT Resource Center*. The Collaboration for NDT Education, Iowa State University. Web. 16 Mar. 2018.

Wang, C-K Chris. *Atoms, Nuclei & Interactions of Ionizing Radiation with Matter*. Cognella Academic Publishing, 2017. Print.

"What are scintillator materials?" *Scintillator Materials Group*. Stanford University, 2009. Web. 13 April 2018.

"X-Ray Mass Attenuation Coefficients – Air, Dry." *X-Ray Mass Attenuation Coefficients Database.* National Institute of Standards and Technology. Web. 19 Mar. 2018.